JCB Journal of Cell Biology

ARTICLE

Selective MAP1LC3C (LC3C) autophagy requires noncanonical regulators and the C-terminal peptide

Megan E. Bischoff[1*], Yuanwei Zang[1,2*], Johnson Chu[1], Adam D. Price[1], Birgit Ehmer[1], Nicholas J. Talbot[1], Michael J. Newbold[1], Anurag Paul[1], Jun-Lin Guan[1], David R. Plas[1], Jarek Meller[3,4,5,6], and Maria F. Czyzyk-Krzeska[1,6,7]

LC3s are canonical proteins necessary for the formation of autophagosomes. We have previously established that two paralogs, LC3B and LC3C, have opposite activities in renal cancer, with LC3B playing an oncogenic role and LC3C a tumor-suppressing role. LC3C is an evolutionary late gene present only in higher primates and humans. Its most distinct feature is a C-terminal 20-amino acid peptide cleaved in the process of glycine 126 lipidation. Here, we investigated mechanisms of LC3C-selective autophagy. LC3C autophagy requires noncanonical upstream regulatory complexes that include ULK3, UVRAG, RUBCN, PIK3C2A, and a member of ESCRT, TSG101. We established that postdivision midbody rings (PDMBs) implicated in cancer stem-cell regulation are direct targets of LC3C autophagy. LC3C C-terminal peptide is necessary and sufficient to mediate LC3C-dependent selective degradation of PDMBs. This work establishes a new noncanonical human-specific selective autophagic program relevant to cancer stem cells.

Introduction

Macroautophagy (autophagy), an essential pathway leading to lysosomal degradation of intracellular organelles, long-lived proteins, and RNAs, is a tightly regulated cellular process of major importance in cancer (White, 2015). Oncogenic autophagy provides nutrients, particularly when the supply from extracellular microenvironments is limited, and contributes to therapy resistance. The tumor-suppressing activity of autophagy compensates for pathological alterations to organelles/proteins (e.g., aged mitochondria generating reactive oxygen species and the resulting DNA damage). Thus, biological activity of autophagy requires selectivity in the recognition of a specific cargo to be targeted for degradation under particular conditions. Selectivity in autophagy results from the activity of cargo receptor proteins that are able to recognize cargo in a ubiquitin-dependent or -independent manner and to bind to the ATG8 family of small proteins that are inserted into the autophagosome membrane (Galluzzi et al., 2017; Zaffagnini and Martens, 2016). Mammalian homologues of ATG8 include three paralogs of microtubule-associated protein 1 light-chain 3 α, β, and γ (LC3A, LC3B, and LC3C, respectively) and members GABA type A receptor–associated proteins (GABARAPs). The ubiquitylated cargo binds to the ubiquitin-binding domains present on several canonical cargo receptors (e.g., p62, NBR1, CALCOCO2-3). In turn, these receptors bind to LC3s or GABARAPs through LC3 interacting region (LIR) motifs. While there are examples of ubiquitin-independent selective autophagy, the mechanisms of cargo recognition are not well understood (Zaffagnini and Martens, 2016).

We established that LC3B- and LC3C-dependent autophagic programs have opposite functions in clear cell renal cell carcinoma (ccRCC) regulated by the von Hippel–Lindau tumor suppressor (VHL), the main tumor suppressor lost in ccRCC (Hall et al., 2014; Mikhaylova et al., 2012). LC3B-mediated autophagy plays a key role in the progression of ccRCC and is inhibited by VHL (Hall et al., 2014; Mikhaylova et al., 2012). In contrast, LC3C autophagy has tumor-suppressing activity in a renal cancer xenograft model and is positively regulated by VHL due to the inhibition of hypoxia-inducible factors, which transcriptionally repress LC3C (Mikhaylova et al., 2012). Thus, VHL orchestrates a shift between tumor-suppressing and oncogenic autophagic programs. Tumor-suppressing activity of LC3C autophagy in renal cancer is further supported by the fact that LC3C activity is induced by folliculin (FLCN), another renal tumor suppressor (Bastola et al., 2013) and that it regulates Met receptor tyrosine

[1]Department of Cancer Biology, University of Cincinnati College of Medicine, Cincinnati, OH; [2]Department of Urology, Qilu Hospital, Shandong University, Jinan, People's Republic of China; [3]Division of Biostatistics and Bioinformatics, Department of Environmental and Public Health Sciences, University of Cincinnati College of Medicine, Cincinnati, OH; [4]Division of Biomedical Informatics, Cincinnati Children's Hospital Medical Center, Cincinnati, OH; [5]Department of Biomedical Informatics, University of Cincinnati College of Medicine, Cincinnati, OH; [6]Department of Pharmacology and Systems Physiology, University of Cincinnati College of Medicine, Cincinnati, OH; [7]Cincinnati Veterans Affairs Medical Center, Department of Veterans Affairs, Cincinnati, OH.

*M.E. Bischoff and Y. Zang contributed equally to this paper; Correspondence to Maria F. Czyzyk-Krzeska: maria.czyzykkrzeska@uc.edu.

kinase– and hepatocyte growth factor–stimulated migration and invasion (Bell et al., 2019). Other known LC3C functions include xenophagy (von Muhlinen et al., 2012), piecemeal mitophagy (Le Guerroué et al., 2017), viral trafficking (Madjo et al., 2016), and exit of proteins from the endoplasmic reticulum (Stadel et al., 2015).

Midbody is a structure built at the intercellular bridge during cytokinesis, forming a platform for the complex process of abscission (White and Glotzer, 2012). After division, the post-division midbody ring (PDMB) is inherited by one of the daughter cells in the case of asymmetric division or by none if the abscission happens on both sides of the midbody and is released into the extracellular space (Crowell et al., 2014; Fazeli and Wehman, 2017; Kuo et al., 2011). Asymmetrically inherited PDMB can undergo macroautophagy (Kuo et al., 2011; Pohl and Jentsch, 2009). PDMBs released outside the cell can be retained on the cell surface and then become phagocytosed (Crowell et al., 2014). In *Drosophila*, asymmetric inheritance of PDMB by female, but not male, germline stem cells is considered a platform for asymmetric segregation of molecules (Salzmann et al., 2014). In cancers, a high number of PDMBs promote reprogramming toward pluripotency and increased tumorigenic potential (Kuo et al., 2011).

Here, we investigated mechanisms that contribute to the selectivity of LC3C tumor-suppressing autophagy. We determined that the LC3C autophagic program requires noncanonical members in the upstream regulatory complexes, including the little-known ULK3 as a part of FP200/ATG13/ULK complex; UVRAG, Rubicon (RUBCN), and PIK3C2A as part of the PI3K complex; and the cargo receptor CALCOCO2. We identified PDMBs as specific LC3C cargo degraded by the lysosome, an implication that LC3C prevents reprogramming toward pluripotency. Most importantly, we show that LC3C C-terminal peptide is necessary and sufficient for the selectivity of LC3C-dependent degradation of PDMBs and for the assembly of the upstream noncanonical complexes with LC3C. We determined that the endosomal sorting complex required for transport (ESCRT)-I member TSG101 is required for the assembly of the upstream regulators with LC3C in a C-terminal peptide–dependent manner. The data establish a new mechanism of human-specific selective autophagy in the degradation of oncogenic cargo.

Results

LC3C and LC3B are independent autophagic programs

LC3C differs from LC3B/A in several important ways (Fig. 1 A). There is a 61% amino acid difference in the two N-terminal α-helices that form the LIR-binding domain as well as CLIR-binding motif that interacts with LIR identified on CALCOCO2 cargo receptor (von Muhlinen et al., 2012). This amino acid difference is sufficient for generation of LC3C-specific antibodies (Fig. S1 A). LC3C is specific only for human and other primates as defined by the presence of the same or similar C-terminal 20-amino acid peptide after G126 that undergoes lipidation during autophagosome formation (https://useast.ensembl.org/Homo_sapiens/Gene/Compara_Tree?anc=37570436;db=core;g=ENSG00000197769;g1=ENSCABG00000021351;r=1:241995490-241999098;t=ENST00000357246; Fig. 1 B).

Similarly to LC3B, LC3C accumulates in response to lysosomal inhibition using chloroquine (CQ) or bafilomycin A1 (BAFA1; Fig. 1, C and D), but LC3C and LC3B mainly form separate vesicles, with only a small fraction colocalized as shown in four different cell lines (Fig. 1 D). Importantly, serum starvation (0.1% serum in the media) causes fast, strong, and long-lasting induction of LC3C mRNA accumulation, while this effect is significantly less strong in the case of LC3B (Fig. 1 E). The importance of LC3C in normal kidney epithelial cells is further underscored by the observation that immortalized human renal proximal tubule epithelial cells (RPTECs) show strong induction of LC3C, but not LC3B, in response to serum starvation (Fig. 1 F). Note that in the case of LC3C, we detect only the LC3C form that accumulates in the presence of CQ or BAFA1 and represents the lipidated, LC3C-II form, while we do not detect full-size LC3C or the LC3C-I. This likely indicates very fast conversion of the full-size LC3C to the lipidated form and a mechanism of regulation that has other rate-limiting steps than glycine lipidation. In addition to VHL, LC3C is also positively regulated by another renal cancer tumor suppressor, FLCN. Reexpression of FLCN in UOK 257 cells, which derive from a human patient with Birt-Hogg-Dubé syndrome and have lost endogenous FLCN, induces LC3C and represses LC3B flux, with only minor changes at the mRNA level (Fig. S1 B). Overall, our data support different mechanisms of regulation and physiological activities of the LC3 paralogs.

LC3C autophagy is regulated by noncanonical upstream complexes

To identify members of LC3C upstream regulatory complexes, we knocked down several members of upstream regulatory and lipidation complexes and determined accumulation of LC3C when cells were grown in 0.1% serum for 48 h and not treated or treated with CQ for 1 h before collection. We determined that ATG5 and ATG16 were necessary for both LC3C and LC3B lipidation (Fig. S1, C and D), and LC3C colocalized with ATG16L1 and ATG5 and PI3P puncta as detected by the EGFP-2xFyve reporter (Fig. S1, E and F), an indication that the lipidating cascade is required for the LC3C autophagic program. We also determined that Beclin 1 (BECN1; Fig. S1 G), but not ATG14 (Fig. S1 H), was necessary for LC3C accumulation. ATG14-independent autophagy requires UVRAG in the PI3K-associated complex (Liang et al., 2006; Liang et al., 2008; Matsunaga et al., 2009). Indeed, knockdown of UVRAG inhibited LC3C autophagic flux but was without significant effect on LC3B autophagy (Fig. 2, A and B). LC3C autophagic flux was rescued by reexpression of exogenous strawberry-tagged (STR) UVRAG to the protein levels of endogenous UVRAG (Fig. 2 C) and was induced by overexpression of exogenous UVRAG (Fig. 2 D). Endogenous UVRAG colocalized with endogenous LC3C (Fig. 2 E) but not LC3B (Fig. 2 F). UVRAG had no effect on LC3C mRNA levels (Fig. 2 G).

UVRAG can function in autophagy and in a related process, LC3-associated phagocytosis (LAP; Martinez et al., 2015). The activity of RUBCN discriminates between these two UVRAG activities. RUBCN is an inhibitor of the BECN1/UVRAG complex in autophagy (Matsunaga et al., 2009), but an activator of the BECN1/UVRAG complex in LAP (Martinez et al., 2015).

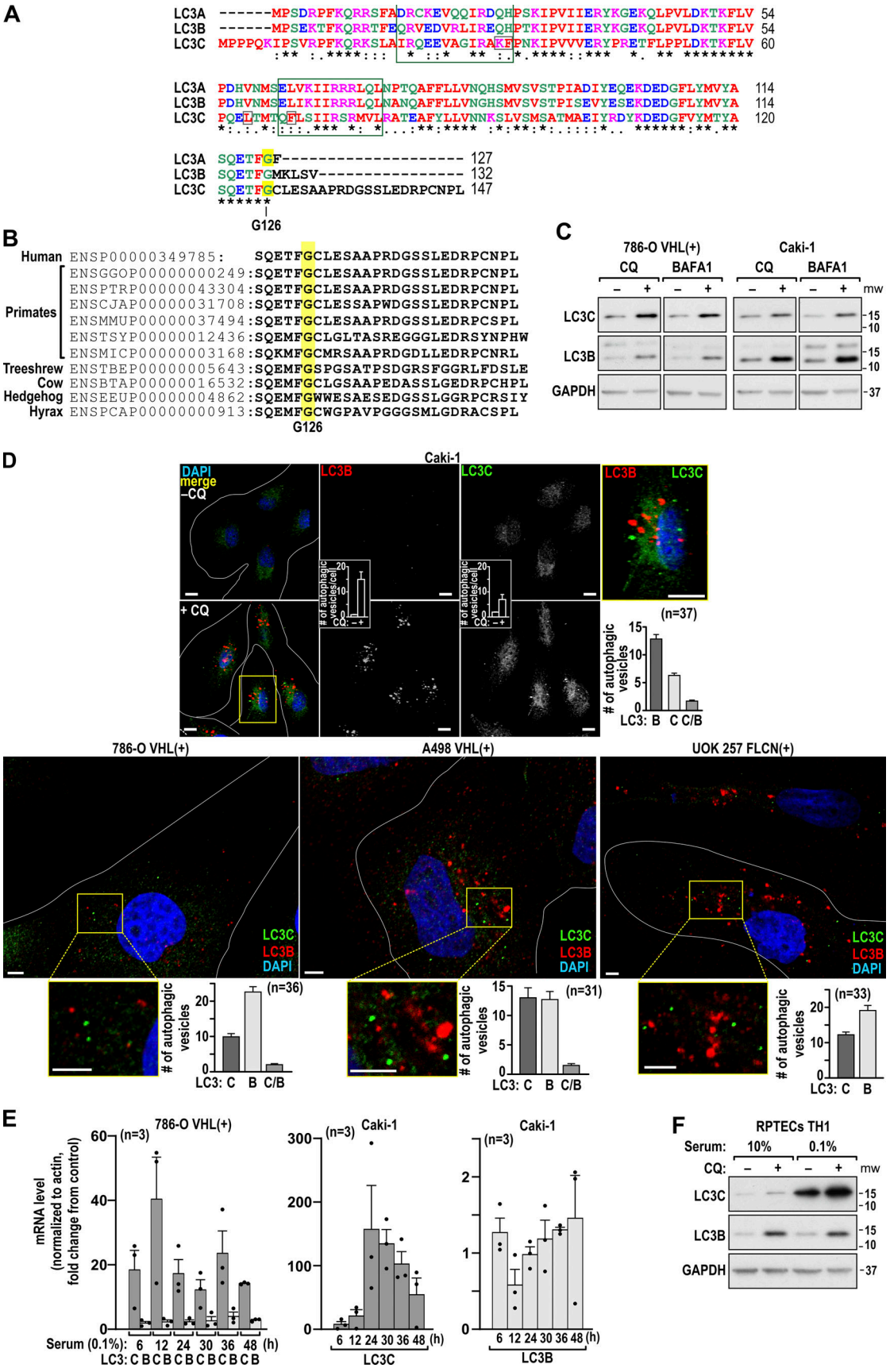

Figure 1. **LC3C and LC3B are separate autophagic programs. (A)** Sequence alignment of LC3 paralogs. Along the bottom, * indicates conserved; ":" conservative; and "." nonconserved changes in amino acid composition. Large green boxes represent α-helices forming the LIR-binding domain for the cargo

receptors. Small gray boxes mark amino acids forming the CLIR-binding site; C-terminal G126, which undergoes lipidation is marked in yellow. **(B)** Sequence of the LC3C C-terminal peptide is conserved among primates and humans but not other species. G126 undergoing lipidation is marked in yellow. **(C)** LC3C and LC3B similarly accumulate in response to 1-h treatment with 100 µM CQ or 200 nM BAFA1. **(D)** Immunofluorescence of LC3C and LC3B puncta with specific antibodies in the indicated cells treated without and with CQ for 1 h to inhibit lysosomal processing. Insets show quantification of puncta in the indicated number of cells. Higher magnification and quantification of the puncta show that only a very small fraction colocalizes. **(E)** Time course showing robust induction of LC3C, but not LC3B, mRNA in response to serum starvation (0.1% serum). For each time point, data are normalized to mRNA measured in cells grown in 10% serum. Serum starvation induction of LC3C mRNA was significantly higher than induction of LC3B mRNA in 786-O VHL(+) cells at P = 0.00138 (by one-way ANOVA) and in Caki-1 at P = 0.0106 (by one-way ANOVA). **(F)** LC3C, but not LC3B, was induced by serum starvation (48 h, 0.1% serum) in human RPTECs. Scale bars = 10 µm. In all bar graphs, mean ± SEM is shown.

Knockdown of RUBCN inhibited LC3C autophagy (Fig. 2, H and I). STR-RUBCN rescued the effects of the knockdown (Fig. 2 J), and RUBCN colocalized with LC3C (Fig. 2 K). There were no effects of RUBCN knockdown on LC3C mRNA (Fig. 2 L).

PIK3C3 is required for canonical activation of autophagy. Surprisingly, LC3C autophagic flux was not affected by the knockdown of PIK3C3 (Fig. S2, A and B). Instead, we determined that a PI3K class II member, PIK3C2A, was necessary for LC3C autophagy (Fig. 3, A and B). The effect of PIK3C2A knockdown was rescued by reexpression of exogenous PIK3C2A (Fig. 3 C). Endogenous PIK3C2A colocalized with LC3C (Fig. 3 D) but not with LC3B (Fig. S2 C). Furthermore, we determined that LC3C colocalized with EGFP-2xFyve, a reporter for PI3P, in a PIK3C2A-dependent, but not PIKC3C-dependent, manner, supporting the role of this lipid and PIK3C2A in the formation of LC3C vesicles (Fig. 3, E and F; and Fig. S2 D). The formation of this complex was supported by coimmunoprecipitation of endogenous BECN1, RUBCN, PIK3C3A, and LC3C with endogenous UVRAG in 786-O VHL(+) and Caki-1 cells (Fig. 3 G). Knockdown of PIK3C2A did not affect LC3C mRNA expression levels (Fig. 3 H).

Analysis of the role of FIP200/ATG13/ULK in LC3C lipidation revealed that LC3C, similarly to LC3B, required FIP200 (Fig. 4, A and B) and ATG13 (Fig. 4, C and D). However, ULK1 and ULK2 were not necessary for LC3C autophagy, although their knockdowns inhibited LC3B autophagy (Fig. 4, E–G). This surprising observation was supported by the fact that expression levels of ULK1 and ULK2 were lower compared with the expression of ULK3 in all cell lines and that ULK2 expression was extremely low in 786-O and A498 VHL(+) cell lines (Fig. 4 H). Consistently, knockdown of ULK3 repressed accumulation of LC3C, but not LC3B, in response to CQ treatment in all cell lines (Fig. 5, A and B). Reexpression of exogenous STR-ULK3 to the same level as endogenous ULK3 rescued LC3C flux (Fig. 5 C). STR-ULK3 colocalized with endogenous LC3C (Fig. 5 D) but not with endogenous LC3B (Fig. 5 E). ULK3 was part of the complexes that include FIP200, ATG13, and LC3C (Fig. 5, F–H). The effects of ULK3 on LC3C did not involve changes in LC3C mRNA levels (Fig. 5 I).

These data implicate tissue-specific activities of ULK3 in renal cells. Overall, these data show that LC3C is an autophagic program regulated by novel noncanonical upstream ULK- and BECN1-associated complexes.

LC3C autophagy targets PDMBs for degradation and prevents their asymmetric inheritance

Previous work showed that ULK3 localizes to the midbody and serves as an abscission checkpoint to assure full separation of DNA into the two daughter cells (Caballe et al., 2015). Consistently, we found that endogenous PDMB proteins MKLP1, CYK4, and CEP55 coimmunoprecipitated with STR-ULK3 (Fig. S3 A). In addition, UVRAG localizes to midbodies (Thoresen et al., 2010). Thus, we hypothesized that LC3C, downstream from ULK3, regulates degradation of PDMBs during serum starvation. We found that under serum starvation conditions that induce LC3C flux (48 h in 0.1% serum), LC3C, but not LC3B, colocalized with PDMBs (Fig. 6, A–C; and Fig. S3 B). Because LC3C is positively regulated by VHL and FLCN, we determined effects of VHL and FLCN on the accumulation of PDMBs. The number of PDMBs in VHL(–) or FLCN(–) RCC cells was high and did not increase by incubation with CQ for 24 h (Fig. 6, D–F). Reconstitution of VHL in VHL(–) RCC cells or of FLCN in FLCN(–) cells lowered the number of PDMBs and recovered regulation by CQ, indicating the degradation of PDMBs by lysosomes (Fig. 6, D and E). In contrast, degradation of PDMBs in cells grown in 10% serum did not depend on *VHL* or *FLCN* status (Fig. S3, C and D), suggesting the existence of different autophagic programs degrading PDMBs under serum-starved and nonstarved conditions. Importantly, knockdown of LC3C, but not LC3B, reversed the effects of VHL or FLCN reconstitutions, resulting in higher constitutive PDMB numbers and lack of regulation by 24-h CQ treatments (Fig. 6, G and H). Knockdown of LC3C-specific upstream regulators ULK3, PIK3C2A, UVRAG, and RUBCN induced numbers of PDMBs similarly to the LC3C knockdowns, supporting their role in degradation of PDMBs (Fig. 6 I). Consistently, there was colocalization of EGFP-2xFyve, a reporter for PI3P, with PDMBs markers that was significantly diminished by knockdown of PIK3C2A but not PIK3C3 (Fig. 6, J and K), further supporting the role PIK3C2A in the autophagic degradation of PDMBs by LC3C. Moreover, we found increased accumulation of the PDMB proteins MKLP1, CYK4, and ARF6 responsible for the integrity of PDMBs in response to 24-h CQ treatment in cells with intact LC3C. In cells with LC3C knocked down, these proteins accumulated at high levels in the absence of CQ, and there was no further induction in response to CQ treatment (Fig. 6, L and M). PDMBs colocalized with lysosomal marker LAMP1 (Fig. 6 N and Fig. S3 E), further supporting their lysosomal degradation. This colocalization was significantly diminished in the absence of LC3C (Fig. 6 O), an indication that LC3C is required for targeting PDMBs to lysosomes.

During cytokinesis, midbodies recruit the ESCRT. ULK3 interacts with the members of the ESCRT during cytokinesis (Caballe et al., 2015), thus we investigated the role of ESCRT proteins in LC3C autophagy. We determined that the ESCRT-I member TSG101 was necessary for the degradation of PDMBs

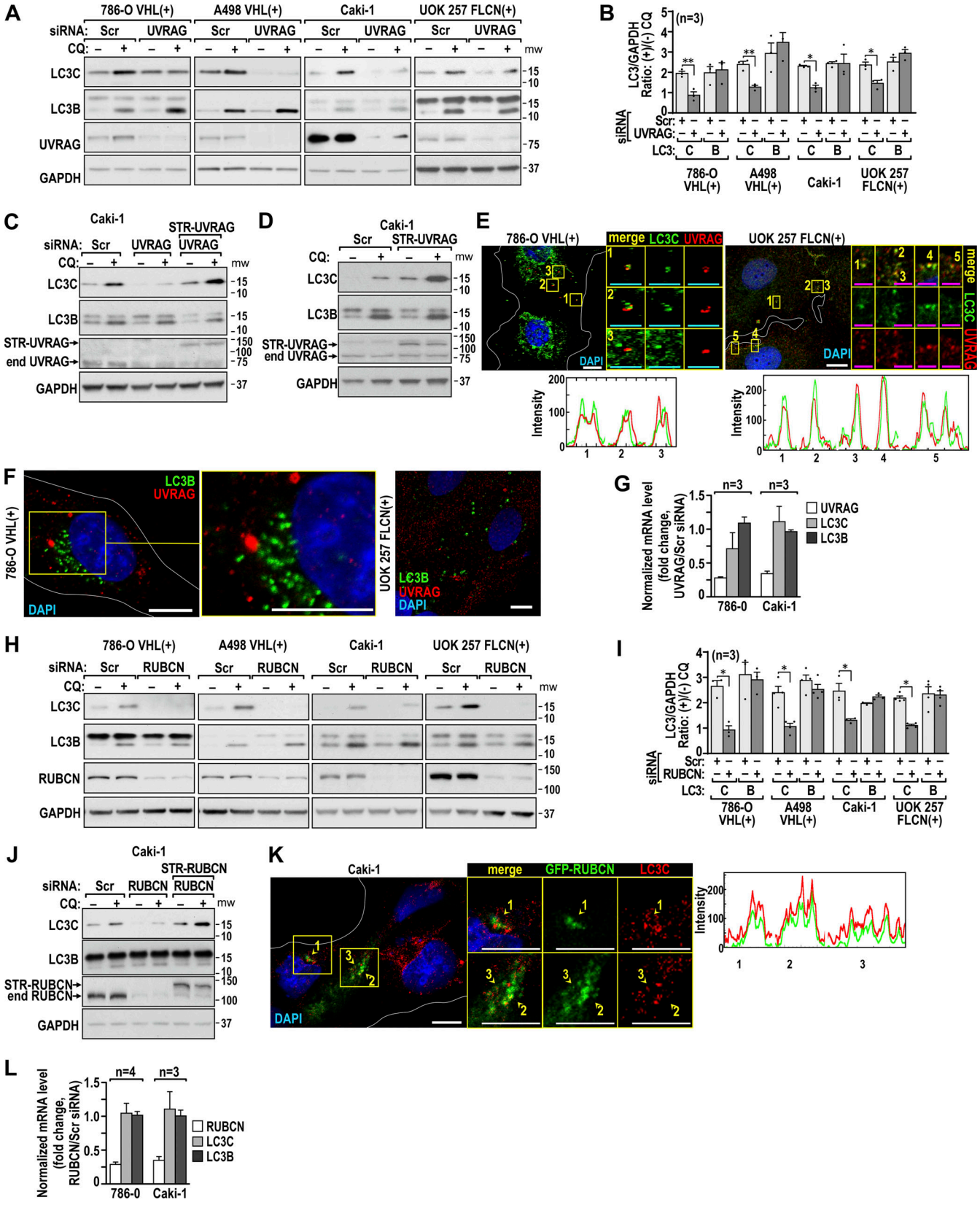

Figure 2. **UVRAG and RUBCN regulate LC3C autophagy. (A)** Immunoblots show a decrease in the CQ-dependent accumulation of LC3C in response to UVRAG knockdown in the indicated cell lines. **(B)** Quantification of the LC3C and B accumulation presented as the ratio of the LC3-II protein levels normalized to GAPDH in CQ(+) versus CQ(−) in cells expressing scrambled (Scr) or UVRAG siRNAs in the indicated cell lines. **(C)** Rescue of LC3C autophagic flux by reexpression of exogenous STR-UVRAG to levels similar to that of endogenous UVRAG (end UVRAG). **(D)** Overexpression of STR-UVRAG induces LC3C autophagic flux. **(E)** STR-UVRAG colocalizes with endogenous LC3C in the indicated cell lines. Split channels and RGB plots are shown below. Cells were treated

with 100 µM CQ for 1 h. **(F)** UVRAG does not colocalize with LC3B under the same conditions that it colocalizes with LC3C. **(G)** RT-PCR data show that LC3C or LC3B mRNA expression was not affected by UVRAG knockdown. **(H)** Immunoblots show a decrease in the CQ-dependent accumulation of LC3C in response to RUBCN knockdown in indicated cell lines. **(I)** Quantification of the LC3C and B accumulation calculated as in B. **(J)** Rescue of the LC3C autophagic flux by reexpression of exogenous STR-RUBCN to levels similar to that of endogenous RUBCN (end RUBCN). **(K)** GFP-RUBCN colocalizes with endogenous LC3C. Split channels and RGB plots are shown. Cells were treated with 100 µM CQ for 1 h. **(L)** RT-PCR data show that LC3C and LC3B mRNA expression was not affected by LC3C or LC3B knockdowns. Scale bars are as follows: white = 10 µm; cyan = 5 µm; magenta = 2.5 µm. In all bar graphs, mean ± SEM is shown. *, $P < 0.05$; **, $P < 0.01$ by unpaired two-tailed *t* test.

(Fig. 6 P). Endogenous TSG101 coimmunoprecipitated endogenous LC3C but not LC3B (Fig. 6 Q). Moreover, TSG101 colocalized with LC3C but not LC3B (Fig. S4, A and B). Knockdowns of TSG101 inhibited LC3C autophagy (Fig. S4 C) and mRNA (Fig. S4 D), pointing to direct and indirect effects of TSG101 on LC3C autophagy and expression.

The inheritance of the cytokinetic midbody from the most recent cell division can be asymmetric if it is maintained by one of the daughter cells (Crowell et al., 2013; Kuo et al., 2011; Salzmann et al., 2014). The inheritance of PDMBs from earlier divisions is not known. Because LC3C degrades PDMBs, we hypothesized that LC3C would increase the number of symmetric divisions, where the PDMB is absent in either daughter cell, with only a new cytokinetic midbody present. Asymmetric division is defined as when one of the daughter cells maintains one or more PDMBs in addition to the cytokinetic midbody (Fig. 7 A). 786-O cells with lost *VHL* had approximately equal numbers of symmetric and asymmetric divisions (Fig. 7 B). In contrast, cells expressing reconstituted *VHL* had significantly higher numbers of symmetric versus asymmetric divisions (Fig. 7 B). Knockdown of *VHL* in Caki-1 cells increased the number of asymmetric divisions (Fig. 7 C). Similarly, cells expressing FLCN had more symmetric divisions compared with cells without *FLCN* (Fig. 7 D). Knockdown of *LC3C* induced a significantly greater number of asymmetric divisions in cells expressing VHL or FLCN (Fig. 7 E; see also Fig. 9 D). The LC3C-dependent clonal inheritance of PDMBs maintenance was further confirmed in cells grown as three-dimensional spheroids. Cells expressing LC3C show low, while cells with LC3C knocked down show high, numbers of inherited PDMBs (Fig. 7, F and G). Importantly, human ccRCCs with mutated *VHL* have higher numbers of PDMBs compared with tumors with WT *VHL* (Fig. 7 H).

Overall, these data provide evidence that the fate of PDMBs, markers of stemness, is under tight control by renal tumor suppressors VHL and FLCN and their downstream target, the LC3C autophagic program.

LC3C autophagy requires the LIR motif on CALCOCO2 and the LIR-binding motif on LC3C

Two major differences between LC3C and LC3B are the CLIR-binding motif in addition to the LIR-binding motif in the N-terminal region and the presence of the C-terminal peptide. Selectivity of LC3C autophagy toward bacterial pathogens requires interaction of LC3C with the CALCOCO2 cargo receptor in a manner that depends on the protein interaction between a specific CLIR motif on CALCOCO2 and a CLIR-binding motif in the N-terminal region of LC3C (von Muhlinen et al., 2012). However, LC3C also contains a LIR-binding site. Thus, we investigated the role of CALCOCO2 and LIR and CLIR motifs in LC3C autophagy. Knockdowns of CALCOCO2, p62, and NBR1 (Fig. S5 A) in cells expressing LC3C demonstrated that only knockdown of CALCOCO2 abolished PDMB degradation, while knockdowns of the other two cargo receptors were without effect (Fig. 8 A). CALCOCO2 colocalized with LC3C (Fig. 8 B) and with PDMBs (Fig. 8, C and D; and Fig. S5 B). Importantly the colocalization of CALCOCO2 with PDMBs was inhibited by LC3C knockdowns (Fig. 8 D). This further supports the idea that LC3C-dependent PDMB degradation is a program independent from the previously described autophagic degradation of midbodies, which requires p62 or NBR1 (Kuo et al., 2011; Pohl and Jentsch, 2009). LC3C with a mutated CLIR-binding motif (Fig. S5 C) rescued lysosomal degradation of PDMBs (Fig. 8 E). Consistently, CALCOCO2 with a mutated CLIR motif (Fig. S5 D) reconstituted in cells with CALCOCO2 knocked down rescued PDMB lysosomal degradation similarly to the WT CALCOCO2 (Fig. 8 F). In contrast, CALCOCO2 with a mutated LIR motif (Fig. S5 D) failed to rescue PDMB lysosomal degradation (Fig. 8 G). This indicates that CALCOCO2 may interact with LC3C through either the LIR or the CLIR (von Muhlinen et al., 2012) motif, most likely depending on the biological context of selective degradation.

LC3C C-terminal peptide is necessary and sufficient for selectivity of LC3C autophagy toward PDMBs

Here, we investigated the role of the C-terminal peptide in selectivity of LC3C autophagy. Reexpression of the autophagy-deficient LC3C G126A mutant (Fig. S5 E) in cells with LC3C knocked down did not rescue lysosomal degradation of PDMBs, further supporting the role of LC3C autophagy in regulation of PDMB fate (Fig. 9 A). Reconstitution of the WT LC3C, but not its short form without the C-terminal peptide (C127Stop; Fig. S5 E), rescued lysosomal degradation of PDMBs (Fig. 9, B and C) and the number of symmetric cells divisions (Fig. 9 D). This indicates that the C-terminal peptide is necessary for LC3C degradation of PDMBs. Interestingly, accumulation of the LC3C C127Stop protein was induced by lysosomal inhibition with CQ. This means that LC3C without the peptide is active in autophagy but likely targets different cargo than the full-size LC3C. To determine whether the C-terminal peptide is sufficient for degradation of PDMBs, we generated a chimeric LC3B–C construct where the C-terminal peptide was added after G120 in LC3B (Fig. S5 F). The chimera was able to restore regulation of PDMBs similarly to what was measured in cells expressing LC3C (Fig. 9 E). Moreover, in cells expressing the chimera, PDMBs colocalized with LC3B or were in close proximity (Fig. 9 F and Fig. S5 G). The chimera construct was expressed at levels similar to the expression of endogenous LC3C as measured by RT-PCR, with primers selective for LC3C and LC3B-C (Fig. 9 G).

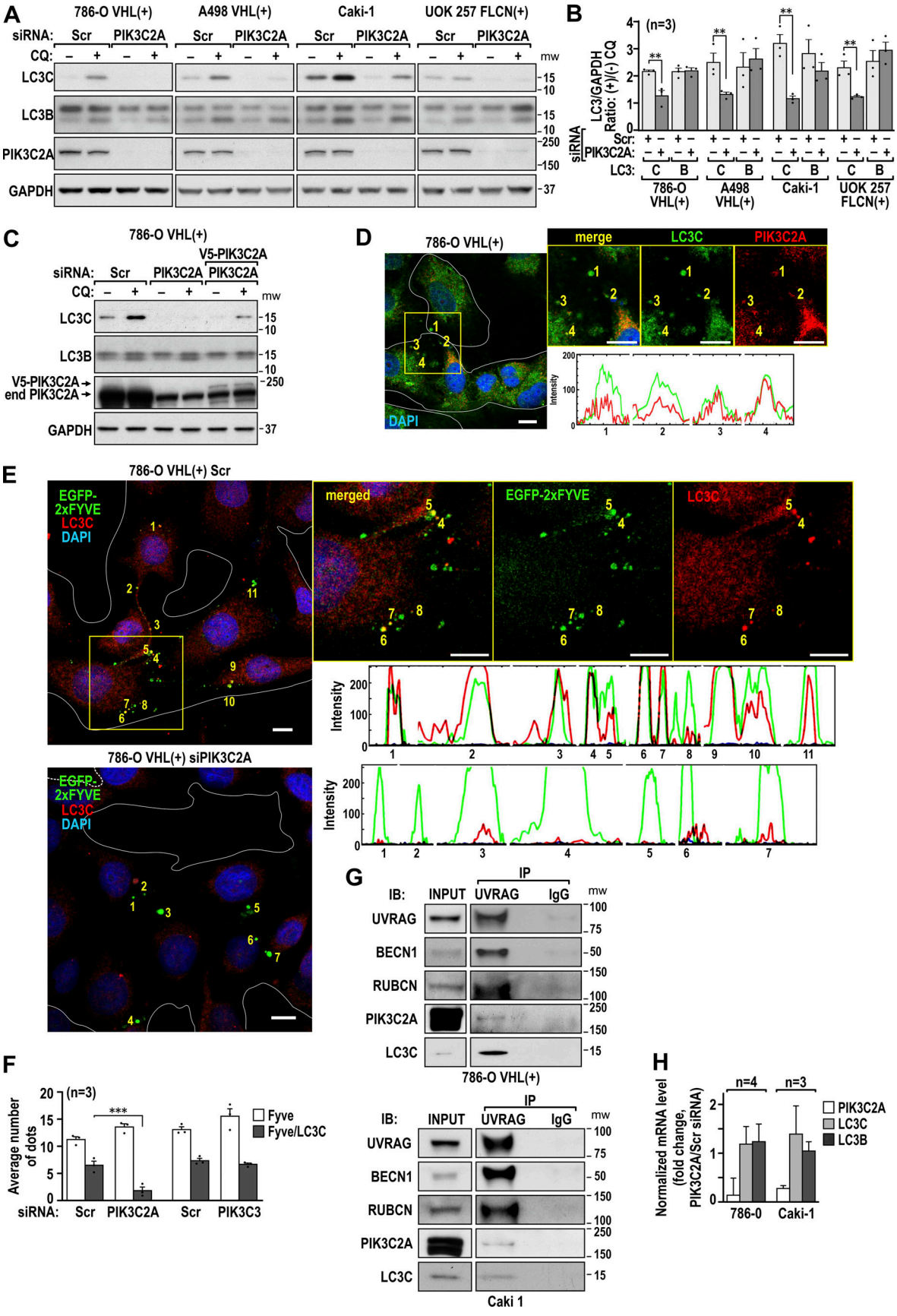

Figure 3. **LC3C noncanonical upstream complexes require PIK3C2A. (A)** Immunoblots show decrease in the CQ-dependent accumulation of LC3C in response to PIK3C2A knockdown in the indicated cell lines. **(B)** Quantification of the LC3C and B accumulation calculated as in Fig. 2 B. **(C)** Rescue of the LC3C

autophagic flux by reexpression of exogenous V5-tagged PIK3C2A. **(D)** Colocalization of PIK3C2A with endogenous LC3C. Examples of RGB profiles and split images are shown. Cells were treated with 100 µM CQ for 1 h. **(E)** Colocalization of LC3C with PI3P reporter EGFP-2xFyve in control cells and loss of this colocalization in cells with PIK3C2A knockdown. Examples of RGB profiles and split images are shown. **(F)** Quantification of LC3C–EGFP-2xFyve colocalization in cells with PIK3C2A and PIK3C3 knockdowns. **(G)** Coimmunoprecipitation of endogenous BECN1, RUBCN, PIK3C2A, and LC3C with endogenous UVRAG in 786-O VHL(+) and Caki-1 cells. **(H)** RT-PCR shows that PIK3C2A knockdown does not affect LC3C or LC3B mRNA expression. Scale bars = 10 µm. In all bar graphs, mean ± SEM is shown. **, P < 0.01; ***, P < 0.001 by unpaired two-tailed *t* test. IB, immunoblot; IP, immunoprecipitation; Scr, scramble.

Next, we sought to determine whether binding of PDMB proteins and formation of the noncanonical complex with LC3C was regulated by the presence of LC3C peptide. We expressed FLAG-tagged LC3C WT and C127Stop and G126A mutants together with TSG101 in HEK293T cells and determined binding of endogenous PDMB proteins and LC3C autophagic regulators by coimmunoprecipitation. Only WT LC3C coimmunoprecipitated with TSG101; all three PDMB markers; and members of the noncanonical upstream complexes ULK3, UVRAG, RUBCN, and PIK3C2A (Fig. 9, H and I). Moreover, the canonical regulators of autophagy FIP200, BECN1, and ATG5-12 conjugate coimmunoprecipitated with both the long and the short form of LC3C, but binding was stronger in the case of LC3C with C-terminal peptide (Fig. 9, H and I). Interestingly, CALCOCO2 bound similarly to the full size and short form of LC3C, indicating that interaction between LC3C and CALCOCO2 is not a major determinant of LC3C selectivity toward PDMBs. Importantly, some upstream regulators, such as ULK3, FIP200, RUBN, and PIK3C2A, bound also to the autophagy-deficient LC3C G126A mutant. This points to a potential sequence in the assembly of the upstream regulatory complexes before processing of LC3C by cleavage and lipidation. Overall, the data indicate that LC3C C-terminal peptide is an important tool of functional selectivity of LC3C autophagy toward PDMBs and is necessary for the assembly of the noncanonical autophagic regulatory complex.

Discussion

Selectivity in the lysosomal degradation of specific cargo under particular biological conditions is essential for maintenance of cellular homeostasis. Our data point to a complex plasticity in LC3C autophagic function that evolved in human cells versus other species. We identified a novel mechanism of selectivity in LC3C autophagy that requires its C-terminal peptide. However, we also noticed that LC3C mutant without the C-terminal peptide, which does not degrade PDMB cargo, accumulates in response to lysosomal inhibition, an indication that this short form of LC3C is engaged in autophagy as well. Moreover, LC3C is able to interact with cargo receptors through LIR- and/or CLIR-binding motifs. This indicates that LC3C can participate in diverse autophagic processes selectively mediated by different utilization of LIR- or CLIR-binding motifs and the absence or presence of the peptide.

We propose that LC3C represents a novel hybrid autophagic program at the intersection of classic autophagy and the endo/phagolysosomal pathway. Clearly, in all four renal cancer–derived cell lines, LC3C required activity of ULK3, rather than ULK1/2, in the complex associated with FIP200/ATG13. The activity of LC3C-dependent autophagy requiring ULK1 has been reported in the case of xenophagy; however, the role of LC3C peptide was not evaluated in these experiments (Ravenhill et al., 2019). Together, these findings further support the role of LC3C as a multifaceted regulator that can require either the ULK3- or the ULK1-associated complex, depending on the biological context.

We have initially determined that LC3C autophagy required BECN1 and the E3-like ATG5/12/16-lipidating cascade. There are two BECN1-associated autophagosome-initiating complexes. Both contain PIK3C3, but complex I includes ATG14, while complex II incorporates UVRAG but not ATG14 (Liang et al., 2006). The activity of the BECN1–UVRAG complex is inhibited by RUBCN (Matsunaga et al., 2009). UVRAG has been shown to stimulate both autophagosome and endosome maturation, promoting lysosomal degradation of cargo independently from its role in autophagosome initiation (Liang et al., 2008). The LC3C requirement for UVRAG supports the role of BECN1-complex II activity; however, surprisingly, RUBCN is a positive regulator of LC3C. This points toward similarity to the recently described BECN1/UVRAG/PIK3C3/LC3B-dependent pathway of LAP where RUBCN is a positive regulator (Lai and Devenish, 2012; Martinez et al., 2016; Martinez et al., 2015; Sanjuan et al., 2007). LAP is not considered a macroautophagic program because it involves formation of a single-membrane structure originating at the plasma membrane to sequester extracellular pathogens and cell debris. It does not require ULK1 but shares several other regulators with autophagy, such as ATG3, ATG5, ATG7, ATG12, and ATG16, which ultimately lead to recruitment of lipidated LC3s on the intravesicular side only, thus preventing recycling of LC3. Pathogens are recognized by plasma membrane receptors, and there is no evidence for ubiquitin modifications. LC3C participates in selective autophagy (xenophagy) of *Salmonella typhimurium* in a mechanism requiring CALCOCO2 and the CLIR motif on CALCOCO2 (von Muhlinen et al., 2012). In contrast to LAP, xenophagy requires formation of a double-membrane autophagosome around a free bacterium in the cytosol, using standard pre- and initiating complexes. The intracellular pathogens are ubiquitylated. However, LAP and xenophagy may have more in common, e.g., fusion of phagosomes with autophagosomes or recruitment of phagosomes as the source of the autophagosome-initiating membrane. Potential involvement of LC3C with a LAP-like program in degradation of PDMBs is supported by the fact that midbodies released during cell division can undergo actin-dependent phagocytosis (Crowell et al., 2014; Fazeli et al., 2016).

The fact that LC3C function requires PIK3C2A and TSG101 further supports LC3C function at the intersection between autophagosome and endosome. Previous work indicated that knockdown of PIK3C2A decreased autophagic output and accumulation of recycling endosomes (Merrill et al., 2017). TSG101 is a member of the ESCRT used by the endolysosomal pathway that

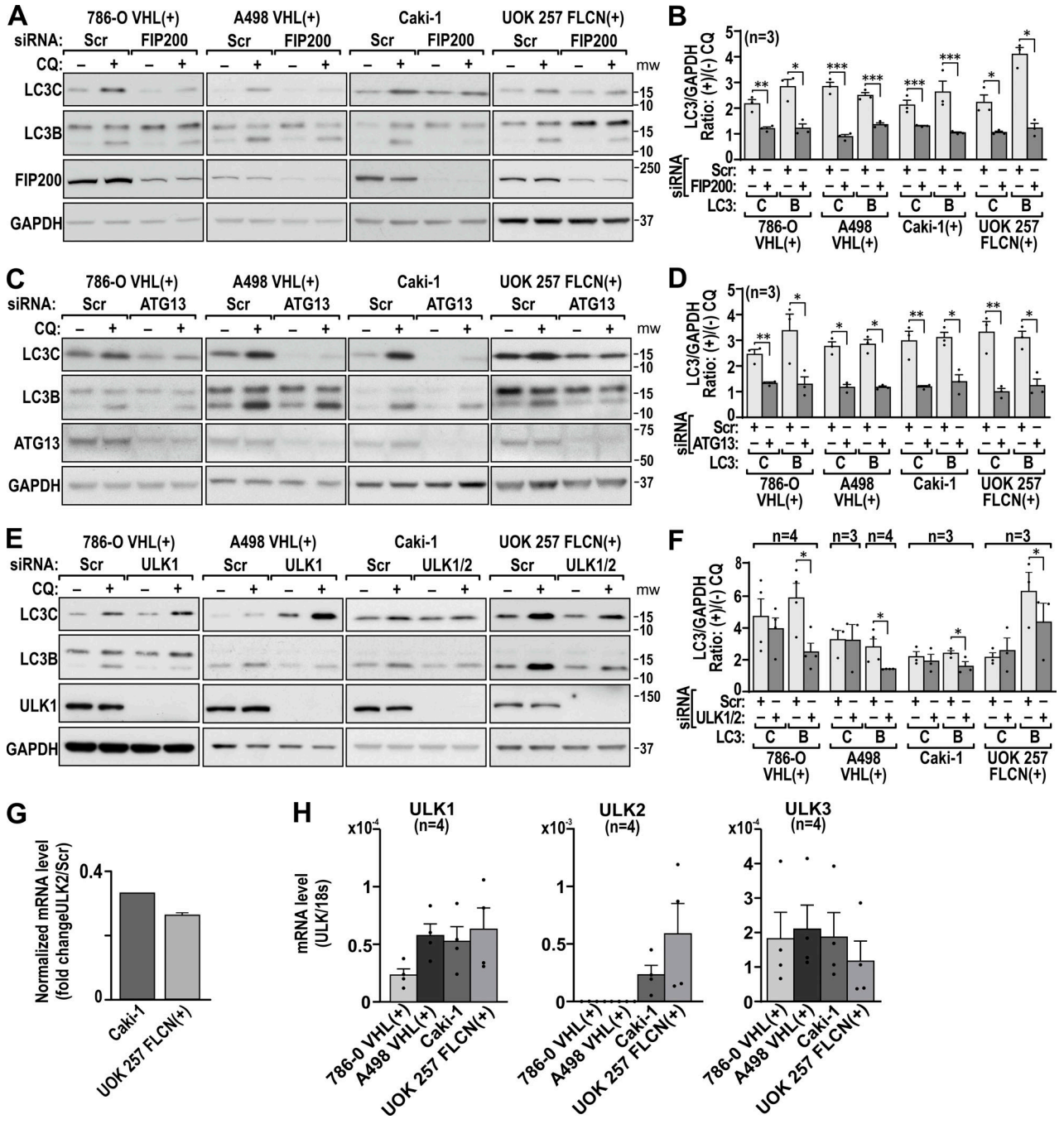

Figure 4. **FIP200 and ATG13, but not ULK1/2, are necessary for LC3C autophagy. (A)** Immunoblots show a decrease in the CQ-dependent accumulation of LC3C and LC3B in response to FIP200 knockdown in indicated cell lines. **(B)** Quantification of the LC3C and B accumulation calculated as in Fig. 2 B. **(C)** Immunoblots show a decrease in the CQ-dependent accumulation of LC3C and LC3B in response to ATG13 knockdown in indicated cell lines. **(D)** Quantification of the LC3C and B accumulation calculated as in Fig. 2 B. **(E)** Immunoblots show lack of effects of ULK1 or ULK1/2 knockdown on LC3C accumulation in response to CQ treatment. **(F)** Quantification of the LC3C and B accumulation calculated as in Fig. 2 B. **(G)** ULK2 knockdown is measured at the mRNA level. **(H)** RT-PCR measurement of mRNA expression of ULK1, ULK2, and ULK3 in the indicated cell lines. In all bar graphs, mean ± SEM is shown. *, $P < 0.05$; **, $P < 0.01$; ***, $P < 0.001$ by unpaired two-tailed *t* test. Scr, scramble.

delivers cargo originating at the plasma membrane or from the extracellular environment via multivesicular bodies. Biogenesis of multivesicular bodies requires a cascade of events regulated by ESCRT to form large numbers of small intraluminal vesicles from the limiting membrane that sort the cargos for lysosomal degradation.

Consistent with the tumor-suppressing activity of LC3C, BECN1 and UVRAG are tumor suppressors and were shown to cooperate to induce autophagy and suppress tumorigenicity of colon cancer cells (Liang et al., 2006). TSG101 and PIK3C2A are favorable prognostic factors in ccRCC according to The Human Protein Atlas. LC3C tumor-suppressing activity targets Met

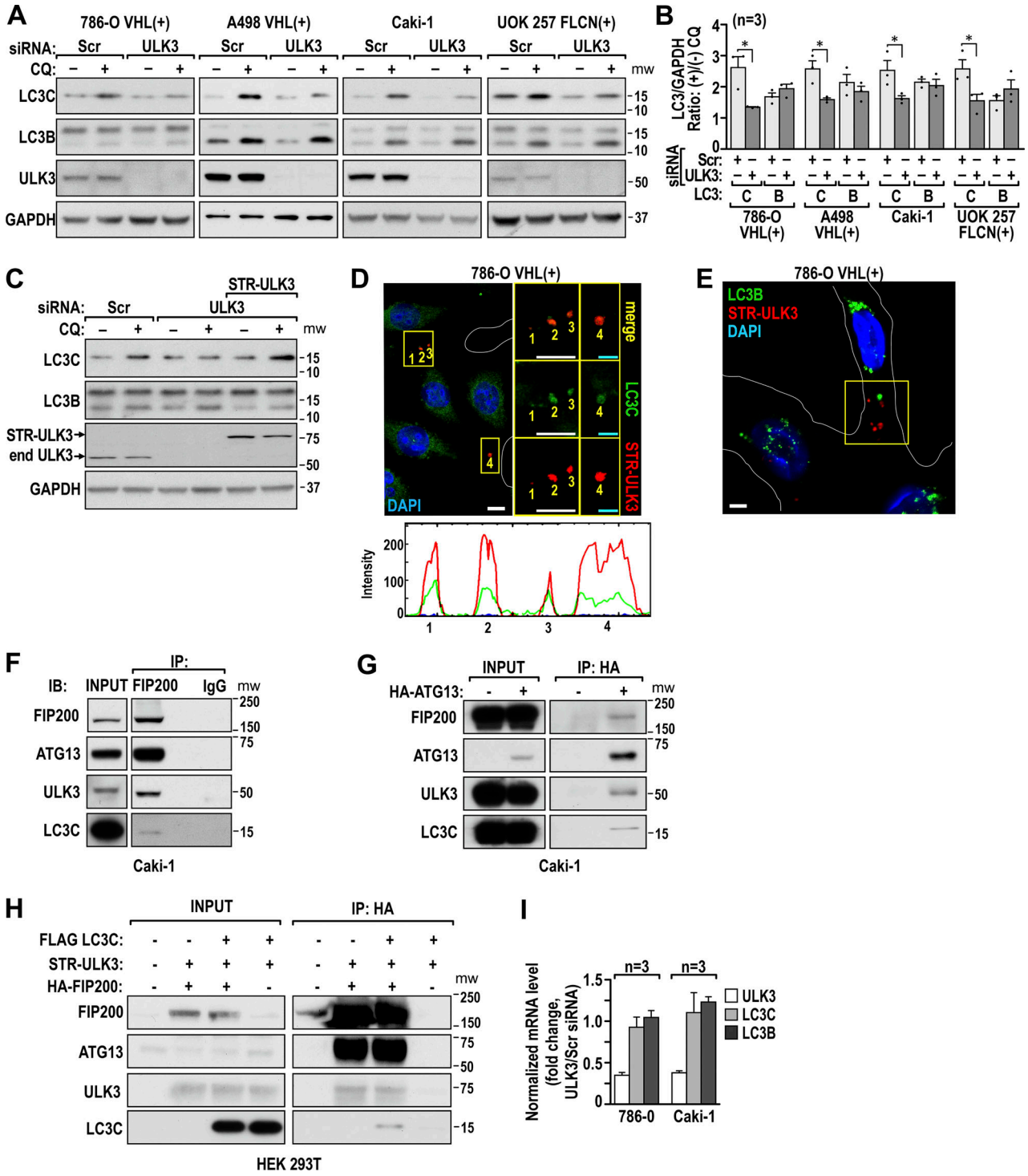

Figure 5. **ULK3 is needed for LC3C autophagy in RCC cells. (A)** Immunoblots show a decrease in the CQ-dependent accumulation of LC3C in response to ULK3 knockdown in indicated cell lines. **(B)** Quantification of LC3C and B accumulation calculated as in Fig. 2 B. **(C)** Rescue of LC3C autophagic flux by re-expression of exogenous STR-ULK3 to levels similar to that of endogenous ULK3 (end ULK3). **(D)** STR-ULK3 colocalizes with endogenous LC3C. Split channels and RGB plots are shown. Cells were treated with 100 µM CQ for 1 h. **(E)** STR-ULK3 does not colocalize with LC3B. **(F)** Coimmunoprecipitation of endogenous ULK3, ATG13, and LC3C with endogenous FIP200 in Caki-1 cells. **(G)** Coimmunoprecipitation of endogenous ULK3, FIP200, and LC3C in Caki-1 cells transfected with HA-ATG13. **(H)** Coimmunoprecipitation of ULK3, ATG13, and LC3C with FIP200 in HEK293T cells transfected with the indicated constructs. **(I)** RT-PCR shows that PIK3C2A knockdown does not affect LC3C or LC3B mRNA expression. Scale bars = 10 µm. In all bar graphs, mean ± SEM is shown. *, $P < 0.05$ by unpaired two-tailed *t* test. IB, immunoblot; IP, immunoprecipitation; Scr, scramble.

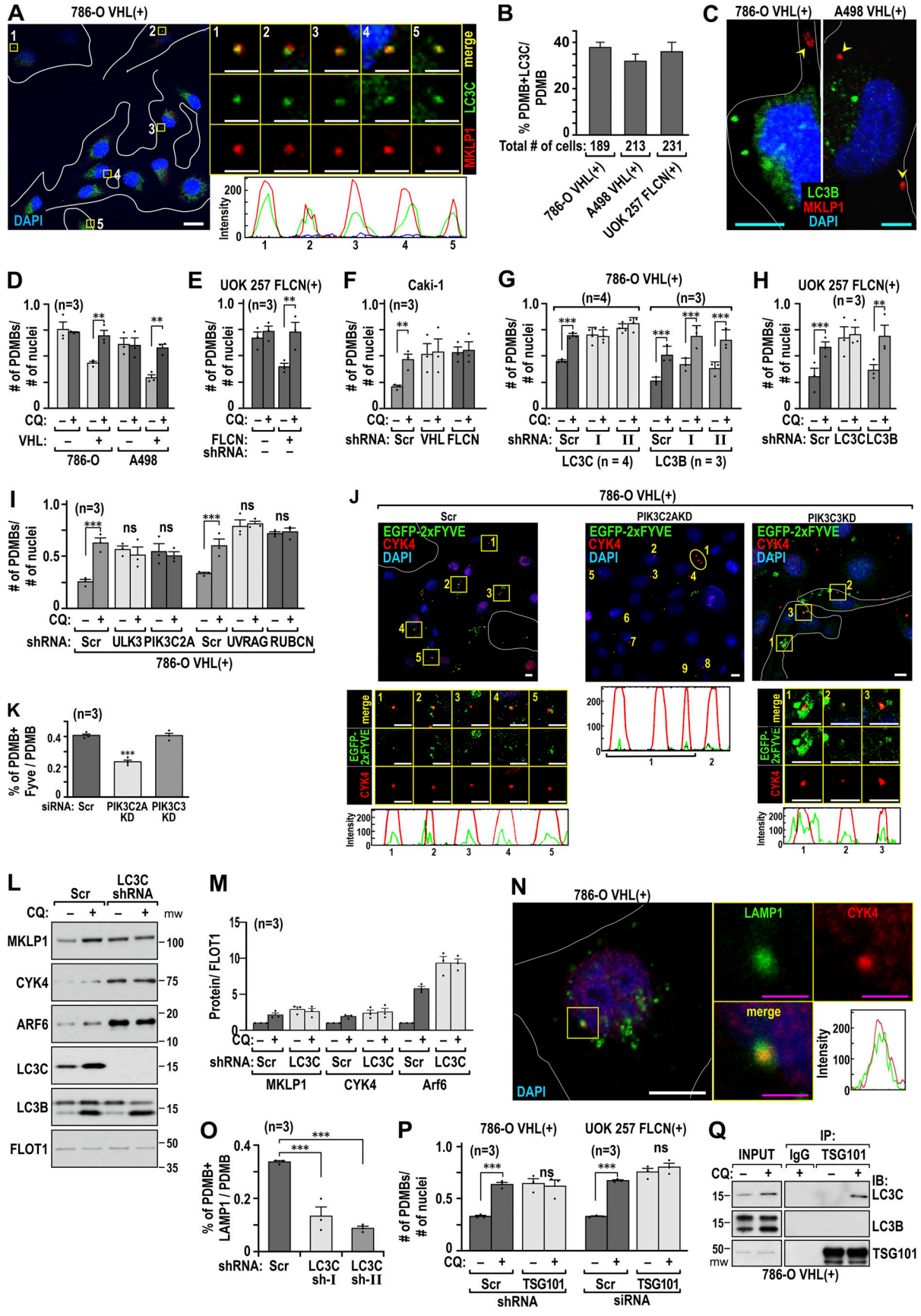

Figure 6. **The LC3C autophagic pathway targets PDMBs for lysosomal degradation. (A)** Endogenous LC3C colocalized with PDMBs, labeled by MKLP antibody. Split channels and RGB plots are shown. Cells were treated with 30 µM CQ for 24 h. **(B)** Quantification of the PDMBs colocalized with LC3C

compared with the total number of PDMBs in the indicated cell lines. **(C)** LC3B did not colocalize with PDMBs. Arrowheads point to the PDMBs. **(D)** Expression of VHL repressed the number of accumulating PDMBs and recovers CQ-dependent accumulation in cell lines without VHL. Ratios of the number of PDMBs to the number of nuclei are shown. Cells were treated 30 µM CQ for 24 h; *n* is the number of independent experiments in which 10 fields with comparable numbers of cells were counted for PDMBs (labeled for MKLP1) and nuclei (DAPI). **(E)** Quantification of PDMBs in the UOK 257 cell line without and with FLCN. **(F)** Quantification of PDMBs in Caki-1 cell line with knockdowns of VHL or FLCN. **(G)** Knockdown of LC3C, but not LC3B, induced the number of PDMBs and abolished CQ-dependent accumulation of PDMBs in 786-O VHL(+) cells. **(H)** Knockdown of LC3C, but not LC3B, induced the number of PDMBs and abolished CQ-dependent accumulation of PDMBs in UOK 257 FLCN(+) cells. **(I)** Knockdowns of LC3C upstream regulators ULK3, PIK3C2A, UVRAG, and RUBCN consistently abolished CQ regulation of PDMBs and increased the number of PDMBs. **(J)** Colocalization of PDMB (CYK4) with PI3P reporter EGFP-2xFyve in cells with PIK3C2A and PIK3C3 knockdowns. Split channels and RGB profiles are shown. **(K)** Quantification of PDMBs colocalized with EGFP-2xFyve in cells shown in J. **(L)** Immunoblot shows CQ-dependent accumulation of PDMB proteins MKLP1, CYK4, and ARF6 in cells with LC3C and CQ-independent accumulation in cells with LC3C knockdown. **(M)** Quantification of immunoblots shown in L from three independent experiments. **(N)** Immunofluorescence experiment shows colocalization of PDMB with LAMP1 lysosomal protein. Split channels and RGB profiles are shown. **(O)** Quantification of colocalization PDMBs with LAMP1 in 786-O VHL(+) cells with and without LC3C. **(P)** Quantification of PDMBs in the indicated cell lines with TSG101 knockdown. **(Q)** Endogenous TSG101 coimmunoprecipitated endogenous LC3C but not LC3B. Cells were treated with 100 µM CQ for 1 h. Scale bars are as follows: white = 10 µm; cyan = 5 µm; magenta = 2.5 µm. In all bar graphs, mean ± SEM is shown. **, P < 0.01; ***, P < 0.001 by unpaired two-tailed *t* test. IB, immunoblot; IP, immunoprecipitation; KD, knockdown; Scr, scramble.

receptor tyrosine kinase and regulates cell migration and invasion (Bell et al., 2019). It remains to be determined whether LC3C autophagy can have both tumor-suppressing and oncogenic activities, depending on the presence or absence of the C-terminal peptide. We established that LC3B has oncogenic activity in ccRCC (Hall et al., 2014; Mikhaylova et al., 2012); thus, expression of short form of LC3C may mimic effects of LC3B.

LC3C-dependent autophagic degradation of PDMBs occurs under low-concentration conditions of serum, which is different from previously reported autophagic degradation of cytokinetic midbodies performed with standard cell culture media containing 10% serum. In those studies, p62 and NBR1 were identified as cargo receptors (Kuo et al., 2011; Pohl and Jentsch, 2009). Moreover, these studies investigated the inheritance of midbodies formed during the most recent cytokinesis (first generation). We, however, investigated inheritance of PDMBs, i.e., midbodies that were formed during previous cytokinesis. Importantly, the maintenance of PDMBs was heritable; clonal spheroids were easily separated into those with high and low PDMB content according to LC3C status. This implies that regulation of PDMBs by LC3C contributes to cell fate reprogramming.

We have demonstrated that the C-terminal peptide is functionally necessary for the degradation of PDMBs and for the assembly of LC3C regulatory complexes. Interestingly, we see exclusively the lipidated form of LC3C that accumulates in response to lysosomal inhibitors and never the noncleaved form, which indicates very fast processing of LC3C to its active form. Recently, evidence was presented for an interaction of TBK1-phosphorylated serines 93 and 96 in the N-terminal region of LC3C with arginine 134 in the peptide, promoting local structuring of the otherwise highly dynamic and unstructured peptide. This interaction diminished the ability of ATG4 to cleave the peptide (Herhaus et al., 2020). These data support the functional and regulatory role of the peptide in LC3C autophagy. We have observed robust transcriptional regulation of LC3C by serum starvation, a condition that induces LC3C autophagy in multiple cell lines (Fig. S1; Mikhaylova et al., 2012). Strong dependence on the continuing input of new LC3C molecules is likely to be necessary in the LC3C autophagy requiring C-terminal peptide, as only the newly translated LC3C will have the peptide, while LC3C that is cleaved from the preexisting autophagosome and reused will not, eliminating functional activity of the peptide. Mechanistic understanding of the regulatory role of the C-terminal peptide will be the subject of future studies.

Materials and methods

Cell lines and basic protocol

Human isogenic VHL(–) and VHL(+) 786-O, A498 cells, Caki-1 cells with endogenous WT VHL and FLCN and their knockdowns, and HEK293T cells were previously described (Bastola et al., 2013; Hall et al., 2014; Mikhaylova et al., 2012). UOK 257 cells have inactivated FLCN. Isogenic cell lines with reconstituted FLCN were a gift from Laura Schmidt (National Cancer Institute, Bethesda, MD). All cells were grown in DMEM/F12 (SH30023; HyClone) with 10% FBS. The human RPTEC (TH1) line was grown in DMEM high-glucose media (SH30022; HyClone) with 10% FBS according to supplier's recommendations. All cell lines are periodically authenticated (Genetica DNA Laboratories), and media are checked monthly for mycoplasma. All relevant reagents are listed in Table S1.

Unless otherwise indicated, experiments were performed according to the following timeline: Cells ($10–30 \times 10^4$) were plated in 60-mm plates in DMEM/F12 medium with 10% serum and allowed to attach. Medium was changed to contain 0.1% serum, and cells were collected 48 h later, with the exception of HEK293T cells that were exposed to 1% serum for 16 h. Knockdowns of indicated genes were performed using si/shRNA the next day after plating followed by 48 h of serum starvation (0.1% serum). To measure autophagic flux, cells were treated with 100 µM CQ or 200 nM BAFA1 for 1–4 h before collection, and for counting PDMBs, cells were treated with 30 µM CQ for 24 h. RNA extractions and quantitative RT-PCR were previously described (Hall et al., 2014; Mikhaylova et al., 2012). For determinations of symmetric and asymmetric cell divisions, cells were placed in 0.1% starvation media as described above and chased with 1% serum in the final 12–16 h before collection. All antibodies, primers, and chemicals used are listed in Table S1.

Transfections and transductions

RCC cell lines were transfected with siRNAs and plasmids using Lipofectamine 3000 according to the manufacturer's protocol.

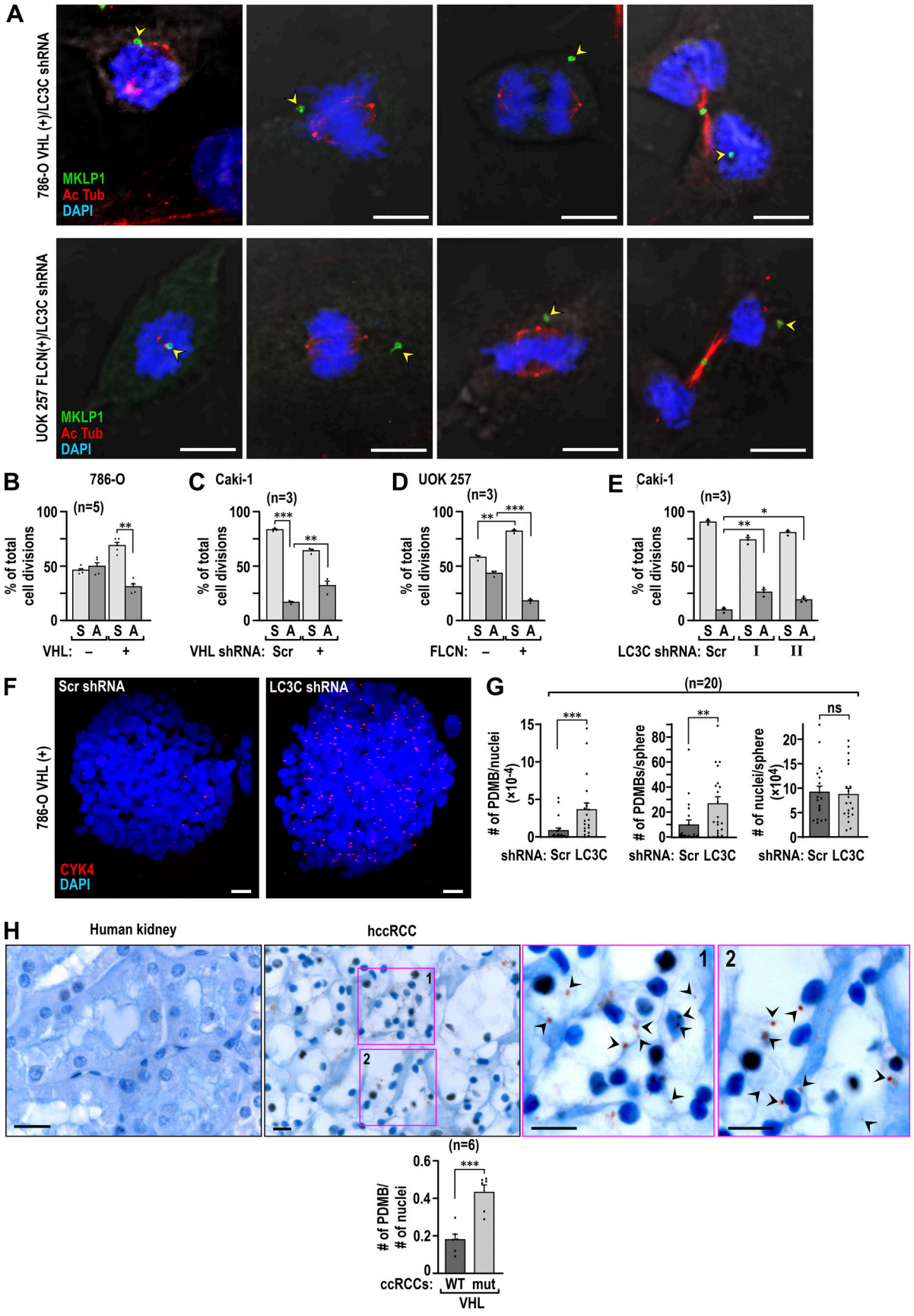

Figure 7. **LC3C inhibits asymmetric inheritance of PDMBs. (A)** Examples of asymmetric cell division in different phases of cell division in 786-O VHL(+) and UOK 257 FLCN(+) LC3C-knockdown cells. Arrowheads point to the PDMBs, which are different from the cytokinetic midbody in the intercellular bridge. Scale

bars = 10 µm. **(B)** Percentage of symmetric and asymmetric cell divisions compared with the total number of cell divisions in 786-O VHL(+) cells without and with reconstituted VHL. **(C)** Percentage of symmetric and asymmetric cell divisions compared with the total number of cell divisions in Caki-1 cells with endogenous VHL and with VHL knocked down. **(D)** Percentage of symmetric and asymmetric cell divisions compared with the total number of cell divisions in UOK 257 cells without and with FLCN. **(E)** Knockdown of LC3C increased the percentage of asymmetric versus symmetric cell divisions compared with the total number of cell divisions in Caki-1 cells with LC3C knocked down. **(F)** 786-O VHL(+) cells with LC3C knockdown grown as three-dimensional spheroids maintained higher levels of PDMBs (CYK staining) in multiple daughter cells. **(G)** Quantification of PDMBs, nuclei, and ratios of PDMBs/nuclei for 20 spheres in each category. Scale bars = 20 µm. **(H)** Immunocytochemistry for PDMBs (CYK4 staining; arrowheads point to PDMBs) and quantification of PDMBs in sections from human normal kidney cells and human ccRCC (hccRCC) cells with WT or mutated (mut) *VHL*. Magnified inset scale bars = 10 µm. In all bar graphs, mean ± SEM is shown. *, P < 0.05; **, P < 0.01; ***, P < 0.001 by unpaired two-tailed *t* test. A, asymmetric; KD, knockdown; S, symmetric; Scr, scramble.

HEK293T cells were transfected using 2 µg polyethylenimine per 1 µg DNA. siRNAs were used at final concentrations of 50 nM or 80 nM. HEK293T cells were transfected with the following amounts of DNA: 100–500 ng of LC3C, 2–5 µg Cherry-TSG101, 2.5 µg GFP-MKLP1, or 0.5 µg STR-ULK3. Viral transductions included addition of 1.1 µg/ml polybrene before viruses were administered. All lentiviral shRNA constructs were VSV-G envelope packaged and 10-fold concentrated (Cincinnati Children's Hospital Medical Center Viral Vector Core) and used at a 1:30 dilution. All controls were treated with empty, nontarget, or scrambled constructs. Media were changed 6–8 h after transfection or the following day after transfection/transduction unless otherwise specified. Stable cell line pools were selected with appropriate antibiotics 2–3 d after transduction and maintained in the selection media.

To achieve similar expression levels compared with endogenous, the following approaches were used: For UVRAG rescue experiments, knockdown of endogenous UVRAG was performed on cells stably expressing STR-UVRAG. For ULK3 and RUBCN rescue experiments, cells were transduced with viral exogenous constructs at 1:5,000 and 1:20,000, respectively, then replated 3 d later for knockdown of the endogenous genes. For PIK3C2A, cells were transfected with 15 µg plasmid PIK3C2A DNA and split 3 d later following knockdown of endogenous gene. For FLAG-LC3C rescue experiments, 50–150 ng plasmid DNA was transfected in stable LC3C knockdowns. For CALCOCO2 reconstitutions, 0.3–0.4 µg DNA was transfected, media were changed to starvation 6–8 h later, and cells were treated with lentiviral-packaged shRNA in the starvation media. In all cases, cells were starved with 0.1% FBS for 48 h before collection. For LC3C rescue with untagged viral constructs, virus was titrated between 1:1,000 and 1:500,000 stably or transiently. For immunofluorescence, 350–850 ng GFP-RUBCN, 250–500 ng GFP/FYVE, or 350–700 ng STR-ULK3 was transfected per well.

Coimmunoprecipitation and immunoblotting experiments

For immunoblot analysis, cells were collected in radioimmunoprecipitation assay buffer (25 mM Tris HCl, pH 7.6, 150 mM NaCl, 1% NP-40, 1% sodium deoxycholate, 0.1% SDS). 10–35 µg of extracts were separated on 3%–8%, 12%, or 4%–12% polyacrylamide gels and transferred onto polyvinylidene difluoride membrane. Blots were probed with relevant antibodies, as listed in Table S1.

For immunoprecipitation, cells were lysed in buffer containing 50 mM Hepes, pH 7.9, 5 mM $MgCl_2$, 150 mM NaCl, 1% glycerol, and 1% IGEPAL, or a buffer containing 50 mM Tris, pH 8.0, 137 mM NaCl, 1 mM $MgCl_2$, 1 mM $CaCl_2$, and 1% NP-40, and protein lysates were incubated with primary antibody in the same buffer with detergent concentration adjusted to 0.2%. 0.5–1 mg of cell lysates in 0.5–1 ml of indicated buffers supplemented with protease/phosphatase were incubated with primary antibodies overnight at 4°C, followed by 1-h incubation with protein A/G or protein G magnetic beads at room temperature. In the case that DynaBeads were used, the beads were incubated with the antibody first, followed by 10-min incubation with cell lysates. Beads were washed in the immunoprecipitation buffer, and coimmunoprecipitated proteins were eluted with 1× LDS sample buffer for 10 min at 45°C. In cases where primary antibodies used for immunoblotting were from the same species as the antibody used for immunoprecipitation, Clean-Blot IP Detection Reagent (HRP) was used in place of a secondary antibody. For each immunoprecipitation reaction, the following amounts of primary antibodies were used: 2 µg of anti-TSG101, 3 µg of anti-HA, 1:200 dilution of anti-STR, either 2 µg or 1:250 of anti-FLAG M2, 1:100 dilution of anti-FIP200, and 1:50 dilution of anti-UVRAG. The amount of control IgG was adjusted to the concentrations of the primary antibodies. Data acquisition and quantification for Western blots was performed using ImageJ 1.52a or Image Studio Lite Ver 5.2 software.

Immunofluorescence and PDMB count

For immunofluorescence analysis, cells plated on glass coverslips were fixed with 4% PFA for 20 min at room temperature or 100% methanol for 5 min at −20°C. PFA-fixed cells were additionally quenched with 50 mM NH_4Cl unless already expressing a fluorescent marker. Cells were permeabilized with 0.3% Triton or 0.1% saponin. Coverslips were blocked with PBS containing either 0.1% Triton or 0.1% saponin and either 3% normal goat serum or 1% BSA for 30 min and incubated with primary antibody for 1 h at 37°C. Coverslips were then washed and incubated with Alexa Fluor–labeled secondary antibodies for 30 min at room temperature. Finally, coverslips were washed and mounted using DAPI Fluoromount-G. Antibodies and concentrations are listed in Table S1. PDMBs were counted based on labeling with anti-MKLP1 or anti-CYK4 antibodies. For each experiment, 10 independent and random fields of view were counted for the numbers of PDMBs and nuclei. Each section had between 10 and 30 cells. Ratios of the number of PDMBs to the number of nuclei from all sections were averaged. Confocal images were acquired on a Zeiss LSM 710 confocal microscope with a Zeiss Axio Observer.Z1 stand and a Zeiss Plan-Apochromat objective (63×/1.4 Oil DIC) using Zeiss ZEN 2010 software at room temperature. The appropriate lasers and emission filters for the respective fluorophores were used in multitracking mode. Widefield

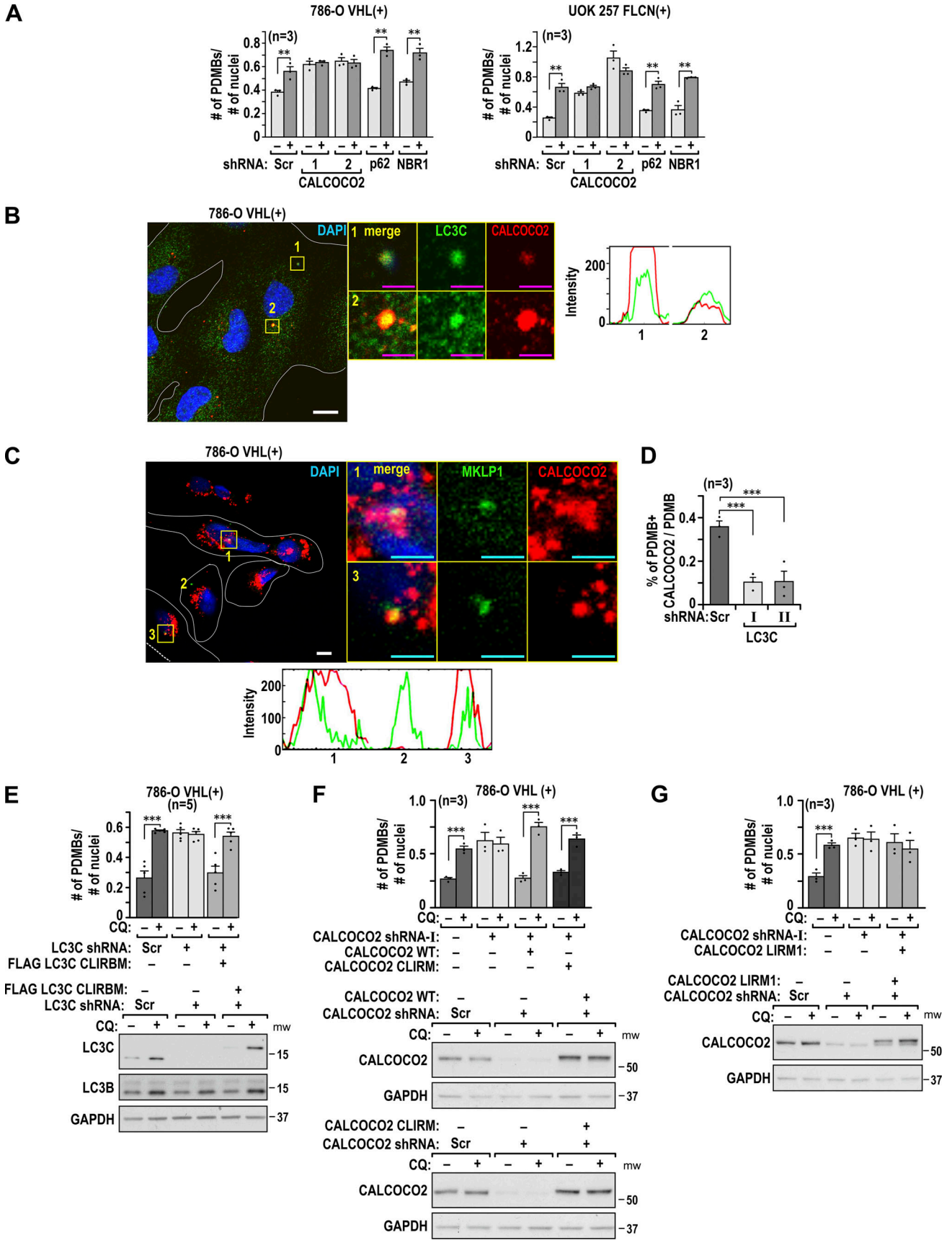

Figure 8. **LC3C autophagy requires CALCOCO2 cargo receptor and LIR motif. (A)** Knockdown of CALCOCO2, but not of p62 or NBR1, abolished CQ-dependent accumulation of PDMBs in the indicated cell lines. **(B)** Colocalization of endogenous LC3C with endogenous CALCOCO2. RGB profiles and split

channels are shown. **(C)** CALCOCO2 colocalized with PDMB. Split channels and RGB profiles are shown. **(D)** Quantification of PDMBs colocalized with CALCOCO2 in cells with and without LC3C. **(E)** FLAG-tagged mutant of the CLIR-binding site on LC3C (CLIRBM) rescued CQ-dependent degradation of PDMBs in cells with LC3C knocked down. Immunoblot shows expression of FLAG-tagged LC3C-CLIRBM at the level of endogenous LC3C. **(F)** CLIR mutant of CALCOCO2 (CLIRM) rescued CQ-dependent degradation of LC3C in cells with CALCOCO2 knocked down, similarly to WT CALCOCO2. Immunoblots show expression of exogenous CALCOCO2 WT and CLIRM matched to the expression of the endogenous CALCOCO2. **(G)** LIR mutant of CALCOCO2 did not rescue CQ-dependent degradation of PDMBs in cells with CALCOCO2 knocked down. Immunoblot shows expression of exogenous CALCOCO2 LIRM matched to the expression of the endogenous CALCOCO2. Analysis of PDMBs was performed as described in Fig. 6 D. Scale bars are as follows: white = 10 µm; cyan = 5 µm. In all bar graphs, mean ± SEM is shown. **, P < 0.01; ***, P < 0.001 by unpaired two-tailed *t* test. Scr, scramble.

images were acquired using a Zeiss Axioplan 2 imaging microscope with the appropriate filter cubes and a Zeiss AxioCam MRm black and white camera to record the images using the Zeiss Axiovision Rel 4.7 software. The objective used had the following specifications: Plan-Apochromat 10/0.45, Plan-Neofluar 20×/0.5, Plan-Neofluar 40×/0.6 (air), Plan-Neofluar 40×/1.3 (Oil), Plan-Apochromat 63×/a.4 (Oil), and α-PlanFluar 100×/1.45. All images were saved as 8-bit images.

Images were also acquired on a Nikon SIMe microscope with a Nikon Eclipse Ti stand using a Hamamatsu C11440 ORCA-Flash4.0 camera and a Nikon SR Apo TIRF 100× SR/1.49 objective at room temperature. The software for acquisition was NIS-Elements Advanced Research version 5.11.00 (64-bit) imaging software by Nikon. DAPI images of nuclei were acquired as widefield images, while we used the structured illumination (SIM) capabilities for the fluorescent channels with a 488-nm, 561-nm, and 640-nm laser line excitation. Red, green, and blue (RGB) profiles (generated by ImageJ 1.53g; Schneider et al., 2012), and split channels are shown.

For determination of symmetric versus asymmetric cell divisions, coverslips were incubated with antibody against MKLP1 to visualize PDMBs and acetylated tubulin to visualize microtubules, and divisions were counted manually under the confocal microscope. For immunocytochemistry, sections of fixed and paraffin-embedded tumors were processed in the Pathology Research Core at Cincinnati Children's Hospital Medical Center and analyzed by light microscopy.

Growth of cells as spheroids

Cells were grown in 8- or 16-well glass chamber slides using a dual chamber coat/culture layer. The floor of each chamber was coated with 100% liquid Matrigel (30–40 µl for 8-well slides and 20 µl for 16-well slides) and allowed to solidify for 30 min in the tissue culture incubator. The culture layer was a 1:1 volume mixture of Matrigel and cells in the plating media (DMEM/F12 and 10% serum). 600 cells were plated in 8-well slides and 200 cells in 16-well slides. After addition of cells, Matrigel was allowed to solidify, and media were added. The next day, media were replaced with fresh plating media. After 4 days, media were changed to the same media containing 0.1% serum. Spheroids were collected after 7–8 d from the time media were changed. For immunofluorescence analysis, spheroids were fixed using 100% methanol for 12 min at −20°C. Spheroids were permeabilized using 0.25% saponin in PBS for 10 min. Spheroids were rinsed with PBS, blocked for 1.5 h using immunofluorescence buffer (PBS, 0.1% saponin, 0.05% T-20, 0.05% NaN_3) with 1% BSA at room temperature and incubated overnight with primary antibodies in immunofluorescence buffer at 4°C. Incubation with secondary antibody in the immunofluorescence buffer was for 1 h at room temperature. Spheroids were washed and mounted using DAPI Fluoromount-G and analyzed by confocal microscopy.

Statistical analysis

Data are expressed as mean ± SEM for three or more independent experiments. Analysis of differential expression was performed using unpaired two-tailed *t* test, with the exception of Fig. 1 E, where one-way ANOVA was used. *, P < 0.05; **, P < 0.01; ***, P < 0.001; and ****, P < 0.0001.

Online supplemental material

Fig. S1 shows regulation of LC3C and LC3B by ATG5, ATG16, and BECN1 and lack of regulation of LC3C by ATG14. Fig. S2 shows lack of regulation of LC3C by PIK3C3. Fig. S3 details additional data regarding regulation of PDMBs by LC3C as supplement to Fig. 6. Fig. S4 illustrates regulation of LC3C by TSG101. Fig. S5 provides additional data supporting results shown in Fig. 8 and Fig. 9. Table S1 provides a list of all reagents used in the study.

Acknowledgments

We thank Dr. C. Wang for reading the manuscript, B. Peace for professional editing, and G. Doerman for preparing the figures.

The work was supported by National Institutes of Health grants R01CA122346 and R01GM128216 and by U.S. Department of Veterans Affairs Biomedical Laboratory Research and Development grant 2I01BX001110 to M.F. Czyzyk-Krzeska. J. Meller was supported by National Institutes of Health grant P30ES006096 and Center for Environmental Genetics grants R01MH107487 and R01DK091566. D.R. Plas was supported by National Institutes of Health grant R01CA168815. J.-L. Guan was supported by National Institutes of Health grants R01NS094144 and R01CA211066. Y. Zang was partially supported by a Shandong University overseas study stipend.

The authors declare no competing financial interests.

Author contributions: M.F. Czyzyk-Krzeska and J. Meller were responsible for the conceptualization and initiation of the project. M.F. Czyzyk-Krzeska was responsible for resources, project administration, supervision, writing, and review and editing. M.E. Bischoff, Y. Zang, J. Chu, A.D. Price, N.J. Talbot, A. Paul, and M.J. Newbold performed experiments and collected and analyzed the data. B. Ehmer was responsible for confocal analysis. J.-L. Guan and D.R. Plas contributed reagents and to the discussion. M.F. Czyzyk-Krzeska, M.E. Bischoff, D.R. Plas, and J.-L. Guan wrote and revised the manuscript. All authors revised the manuscript.

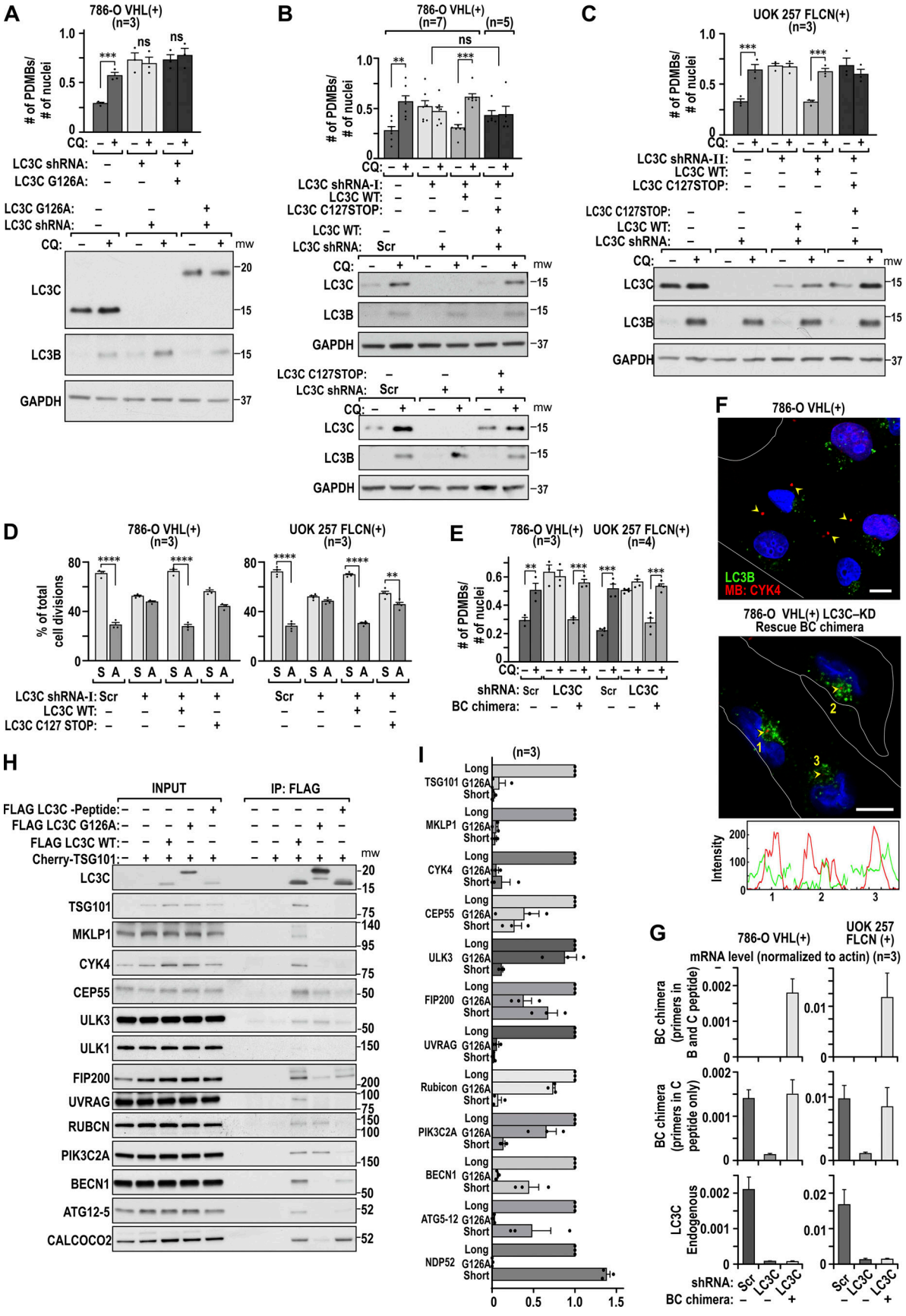

Figure 9. **LC3C C-terminal peptide is necessary and sufficient for selectivity of LC3C autophagy toward PDMBs. (A)** Expression of autophagy-defective mutant of LC3C G126A in cells with LC3C knocked down does not rescue PDMBs degradation. Immunoblot shows expression of LC3C mutant.

(B) Reconstitution of LC3C WT, but not the C127Stop without the LC3C peptide, in 786-O VHL(+) cells rescues PDMB degradation. Immunoblots show levels of expression of exogenous LC3C that match levels of endogenous LC3C. **(C)** Reconstitution of LC3C WT, but not the C127Stop without the LC3C peptide, in UOK 257 FLCN(+) cells rescues PDMB degradation. Immunoblots show levels of expression of exogenous LC3C matching levels of endogenous LC3C. **(D)** Expression of WT LC3C, but not the C127stop mutant, rescues the number of symmetric divisions in the indicted cell lines. **(E)** Expression of LC3B-LC3C C-terminal peptide chimera rescues regulation of PDMBs by lysosomal degradation. **(F)** Representative examples of immunofluorescence experiments showing lack of colocalization of PDMBs with LC3B in cells with LC3C knockdown (top) but appearance of close proximity and colocalization in cells expressing BC chimeras (bottom). RGB profiles are shown. **(G)** RT-PCR quantification of mRNA expression levels using primers specific for the BC chimeras only (top), primers detecting levels of mRNAs containing C-terminal peptide only (middle), and primers specific for LC3C only (bottom). Experiments were done in two indicated cell lines. **(H)** Coimmunoprecipitation of FLAG-tagged LC3C WT and C127Stop mutants with endogenous PDMB proteins in the presence of coexpressed Cherry-TSG101. Experiments were performed in HEK293T cells. **(I)** Quantification of the experiments shown in G. In all bar graphs, mean ± SEM is shown. **, $P < 0.01$; ***, $P < 0.001$; ****, $P < 0.0001$ by unpaired two-tailed *t* test. Scale bar = 10 µm. A, asymmetric; IP, immunoprecipitation; KD, knockdown; S, symmetric; Scr, scramble.

Submitted: 21 April 2020
Revised: 2 March 2021
Accepted: 19 April 2021

References

Bastola, P., Y. Stratton, E. Kellner, O. Mikhaylova, Y. Yi, M.A. Sartor, M. Medvedovic, J. Biesiada, J. Meller, and M.F. Czyzyk-Krzeska. 2013. Folliculin contributes to VHL tumor suppressing activity in renal cancer through regulation of autophagy. *PLoS One.* 8:e70030. https://doi.org/10.1371/journal.pone.0070030

Bell, E.S., P.P. Coelho, C.D.H. Ratcliffe, C.V. Rajadurai, P. Peschard, R. Vaillancourt, D. Zuo, and M. Park. 2019. LC3C-mediated autophagy selectively regulates the Met RTK and HGF-stimulated migration and invasion. *Cell Rep.* 29:4053–4068.e6. https://doi.org/10.1016/j.celrep.2019.11.063

Caballe, A., D.M. Wenzel, M. Agromayor, S.L. Alam, J.J. Skalicky, M. Kloc, J.G. Carlton, L. Labrador, W.I. Sundquist, and J. Martin-Serrano. 2015. ULK3 regulates cytokinetic abscission by phosphorylating ESCRT-III proteins. *eLife.* 4:e06547. https://doi.org/10.7554/eLife.06547

Crowell, E.F., J.Y. Tinevez, and A. Echard. 2013. A simple model for the fate of the cytokinesis midbody remnant: implications for remnant degradation by autophagy. *BioEssays.* 35:472–481. https://doi.org/10.1002/bies.201200132

Crowell, E.F., A.L. Gaffuri, B. Gayraud-Morel, S. Tajbakhsh, and A. Echard. 2014. Engulfment of the midbody remnant after cytokinesis in mammalian cells. *J. Cell Sci.* 127:3840–3851. https://doi.org/10.1242/jcs.154732

Fazeli, G., and A.M. Wehman. 2017. Safely removing cell debris with LC3-associated phagocytosis. *Biol. Cell.* 109:355–363. https://doi.org/10.1111/boc.201700028

Fazeli, G., M. Trinkwalder, L. Irmisch, and A.M. Wehman. 2016. C. elegans midbodies are released, phagocytosed and undergo LC3-dependent degradation independent of macroautophagy. *J. Cell Sci.* 129:3721–3731. https://doi.org/10.1242/jcs.190223

Galluzzi, L., E.H. Baehrecke, A. Ballabio, P. Boya, J.M. Bravo-San Pedro, F. Cecconi, A.M. Choi, C.T. Chu, P. Codogno, M.I. Colombo, et al. 2017. Molecular definitions of autophagy and related processes. *EMBO J.* 36:1811–1836. https://doi.org/10.15252/embj.201796697

Hall, D.P., N.G. Cost, S. Hegde, E. Kellner, O. Mikhaylova, Y. Stratton, B. Ehmer, W.A. Abplanalp, R. Pandey, J. Biesiada, et al. 2014. TRPM3 and miR-204 establish a regulatory circuit that controls oncogenic autophagy in clear cell renal cell carcinoma. *Cancer Cell.* 26:738–753. https://doi.org/10.1016/j.ccell.2014.09.015

Herhaus, L., R.M. Bhaskara, A.H. Lystad, U. Gestal-Mato, A. Covarrubias-Pinto, F. Bonn, A. Simonsen, G. Hummer, and I. Dikic. 2020. TBK1-mediated phosphorylation of LC3C and GABARAP-L2 controls autophagosome shedding by ATG4 protease. *EMBO Rep.* 21:e48317. https://doi.org/10.15252/embr.201948317

Kuo, T.C., C.T. Chen, D. Baron, T.T. Onder, S. Loewer, S. Almeida, C.M. Weismann, P. Xu, J.M. Houghton, F.B. Gao, et al. 2011. Midbody accumulation through evasion of autophagy contributes to cellular reprogramming and tumorigenicity. *Nat. Cell Biol.* 13:1214–1223. https://doi.org/10.1038/ncb2332

Lai, S.C., and R.J. Devenish. 2012. LC3-associated phagocytosis (LAP): connections with host autophagy. *Cells.* 1:396–408. https://doi.org/10.3390/cells1030396

Le Guerroué, F., F. Eck, J. Jung, T. Starzetz, M. Mittelbronn, M. Kaulich, and C. Behrends. 2017. Autophagosomal content profiling reveals an LC3C-dependent piecemeal mitophagy pathway. *Mol. Cell.* 68:786–796.e6. https://doi.org/10.1016/j.molcel.2017.10.029

Liang, C., P. Feng, B. Ku, I. Dotan, D. Canaani, B.H. Oh, and J.U. Jung. 2006. Autophagic and tumour suppressor activity of a novel Beclin1-binding protein UVRAG. *Nat. Cell Biol.* 8:688–699. https://doi.org/10.1038/ncb1426

Liang, C., J.S. Lee, K.S. Inn, M.U. Gack, Q. Li, E.A. Roberts, I. Vergne, V. Deretic, P. Feng, C. Akazawa, and J.U. Jung. 2008. Beclin1-binding UVRAG targets the class C Vps complex to coordinate autophagosome maturation and endocytic trafficking. *Nat. Cell Biol.* 10:776–787. https://doi.org/10.1038/ncb1740

Madjo, U., O. Leymarie, S. Frémont, A. Kuster, M. Nehlich, S. Gallois-Montbrun, K. Janvier, and C. Berlioz-Torrent. 2016. LC3C contributes to Vpu-mediated antagonism of BST2/Tetherin restriction on HIV-1 release through a non-canonical autophagy pathway. *Cell Rep.* 17:2221–2233. https://doi.org/10.1016/j.celrep.2016.10.045

Martinez, J., R.K. Malireddi, Q. Lu, L.D. Cunha, S. Pelletier, S. Gingras, R. Orchard, J.L. Guan, H. Tan, J. Peng, et al. 2015. Molecular characterization of LC3-associated phagocytosis reveals distinct roles for Rubicon, NOX2 and autophagy proteins. *Nat. Cell Biol.* 17:893–906. https://doi.org/10.1038/ncb3192

Martinez, J., L.D. Cunha, S. Park, M. Yang, Q. Lu, R. Orchard, Q.Z. Li, M. Yan, L. Janke, C. Guy, et al. 2016. Noncanonical autophagy inhibits the autoinflammatory, lupus-like response to dying cells. *Nature.* 533:115–119. https://doi.org/10.1038/nature17950

Matsunaga, K., T. Saitoh, K. Tabata, H. Omori, T. Satoh, N. Kurotori, I. Maejima, K. Shirahama-Noda, T. Ichimura, T. Isobe, et al. 2009. Two Beclin 1-binding proteins, Atg14L and Rubicon, reciprocally regulate autophagy at different stages. *Nat. Cell Biol.* 11:385–396. https://doi.org/10.1038/ncb1846

Merrill, N.M., J.L. Schipper, J.B. Karnes, A.L. Kauffman, K.R. Martin, and J.P. MacKeigan. 2017. PI3K-C2α knockdown decreases autophagy and maturation of endocytic vesicles. *PLoS One.* 12:e0184909. https://doi.org/10.1371/journal.pone.0184909

Mikhaylova, O., Y. Stratton, D. Hall, E. Kellner, B. Ehmer, A.F. Drew, C.A. Gallo, D.R. Plas, J. Biesiada, J. Meller, and M.F. Czyzyk-Krzeska. 2012. VHL-regulated MiR-204 suppresses tumor growth through inhibition of LC3B-mediated autophagy in renal clear cell carcinoma. *Cancer Cell.* 21:532–546. https://doi.org/10.1016/j.ccr.2012.02.019

Pohl, C., and S. Jentsch. 2009. Midbody ring disposal by autophagy is a post-abscission event of cytokinesis. *Nat. Cell Biol.* 11:65–70. https://doi.org/10.1038/ncb1813

Ravenhill, B.J., K.B. Boyle, N. von Muhlinen, C.J. Ellison, G.R. Masson, E.G. Otten, A. Foeglein, R. Williams, and F. Randow. 2019. The cargo receptor NDP52 initiates selective autophagy by recruiting the ULK complex to cytosol-invading bacteria. *Mol. Cell.* 74:320–329.e6. https://doi.org/10.1016/j.molcel.2019.01.041

Salzmann, V., C. Chen, C.Y. Chiang, A. Tiyaboonchai, M. Mayer, and Y.M. Yamashita. 2014. Centrosome-dependent asymmetric inheritance of the midbody ring in Drosophila germline stem cell division. *Mol. Biol. Cell.* 25:267–275. https://doi.org/10.1091/mbc.e13-09-0541

Sanjuan, M.A., C.P. Dillon, S.W. Tait, S. Moshiach, F. Dorsey, S. Connell, M. Komatsu, K. Tanaka, J.L. Cleveland, S. Withoff, and D.R. Green. 2007. Toll-like receptor signalling in macrophages links the autophagy pathway to phagocytosis. *Nature.* 450:1253–1257. https://doi.org/10.1038/nature06421

Schneider, C.A., W.S. Rasband, and K.W. Eliceiri. 2012. NIH Image to ImageJ: 25 years of image analysis. *Nat. Methods.* 9:671–675. https://doi.org/10.1038/nmeth.2089

Stadel, D., V. Millarte, K.D. Tillmann, J. Huber, B.C. Tamin-Yecheskel, M. Akutsu, A. Demishtein, B. Ben-Zeev, Y. Anikster, F. Perez, et al. 2015. TECPR2 cooperates with LC3C to regulate COPII-dependent ER export. *Mol. Cell.* 60:89–104. https://doi.org/10.1016/j.molcel.2015.09.010

Thoresen, S.B., N.M. Pedersen, K. Liestøl, and H. Stenmark. 2010. A phosphatidylinositol 3-kinase class III sub-complex containing VPS15, VPS34, Beclin 1, UVRAG and BIF-1 regulates cytokinesis and degradative endocytic traffic. *Exp. Cell Res.* 316:3368–3378. https://doi.org/10.1016/j.yexcr.2010.07.008

von Muhlinen, N., M. Akutsu, B.J. Ravenhill, Á. Foeglein, S. Bloor, T.J. Rutherford, S.M. Freund, D. Komander, and F. Randow. 2012. LC3C, bound selectively by a noncanonical LIR motif in NDP52, is required for antibacterial autophagy. *Mol. Cell.* 48:329–342. https://doi.org/10.1016/j.molcel.2012.08.024

White, E. 2015. The role for autophagy in cancer. *J. Clin. Invest.* 125:42–46. https://doi.org/10.1172/JCI73941

White, E.A., and M. Glotzer. 2012. Centralspindlin: at the heart of cytokinesis. *Cytoskeleton (Hoboken).* 69:882–892. https://doi.org/10.1002/cm.21065

Zaffagnini, G., and S. Martens. 2016. Mechanisms of selective autophagy. *J. Mol. Biol.* 428(9 Pt A):1714–1724. https://doi.org/10.1016/j.jmb.2016.02.004

Supplemental material

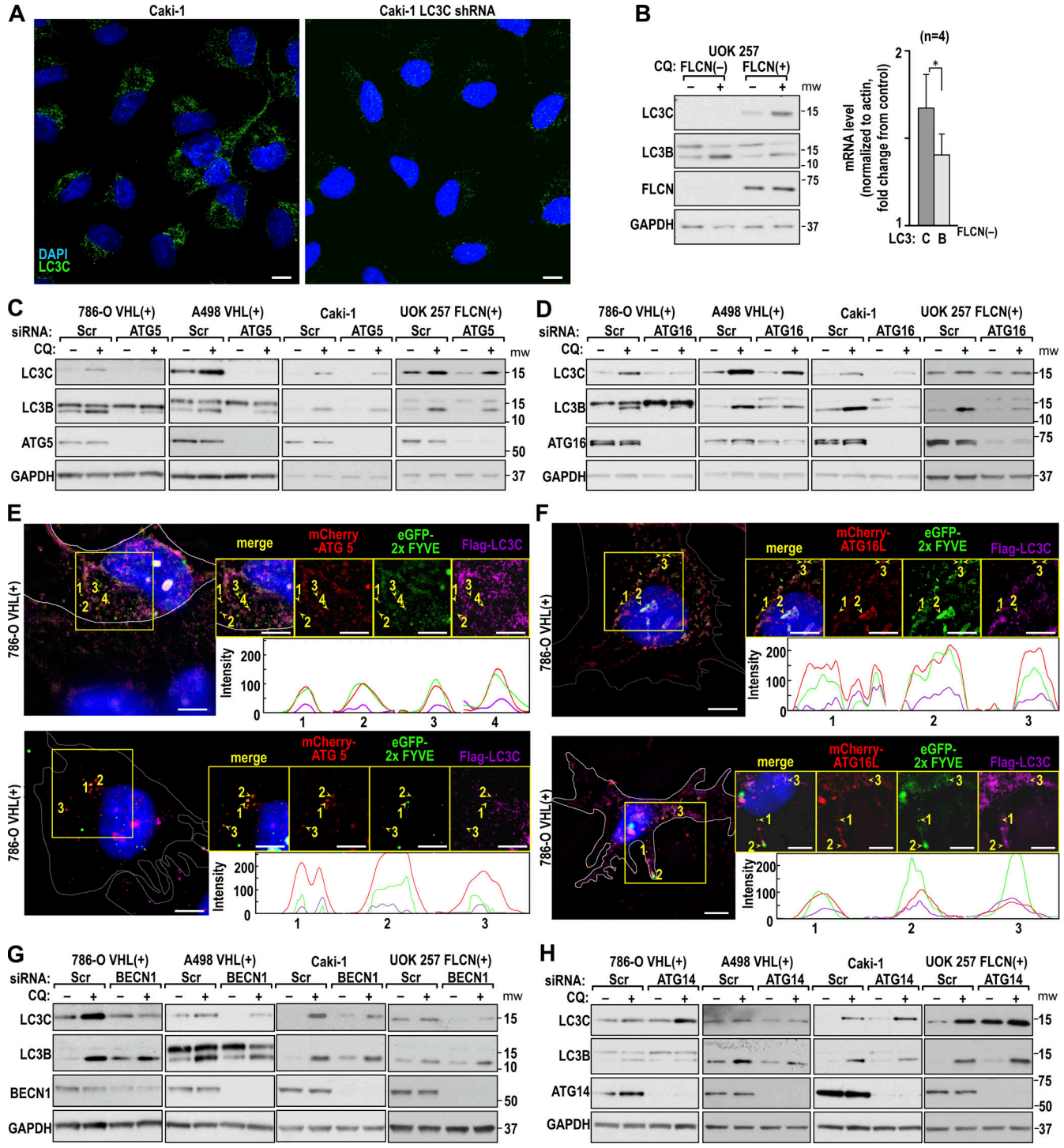

Figure S1. **LC3C autophagy requires ATG5, ATG16, and BECN1 but not ATG14. (A)** Specificity of the anti-LC3C antibody in Caki-1 cells expressing endogenous LC3C or with stably knocked down LC3C. **(B)** Reexpression of FLCN in UOK 257 cells with lost *FLCN* induces LC3C autophagy. **(C)** Knockdown of ATG5 inhibits LC3C autophagy in the indicated cell lines. **(D)** Colocalization of LC3C with ATG5 and GFP-2xFyve puncta as analyzed by SIM. Examples of RGB profiles and split images are shown. **(E)** Knockdown of ATG16 inhibits LC3C autophagy in the indicated cell lines. **(F)** Colocalization of LC3C with ATG16L and GFP-2xFyve puncta as analyzed by SIM. Examples of RGB profiles and split images are shown. **(G)** LC3C flux is inhibited in response to BECN1 knockdown. **(H)** LC3C flux is not inhibited in response to ATG14 knockdown. Scale bars = 10 µm. For bar graph, mean ± SEM is shown. *, $P < 0.05$ by unpaired two-tailed *t* test. Scr, scramble.

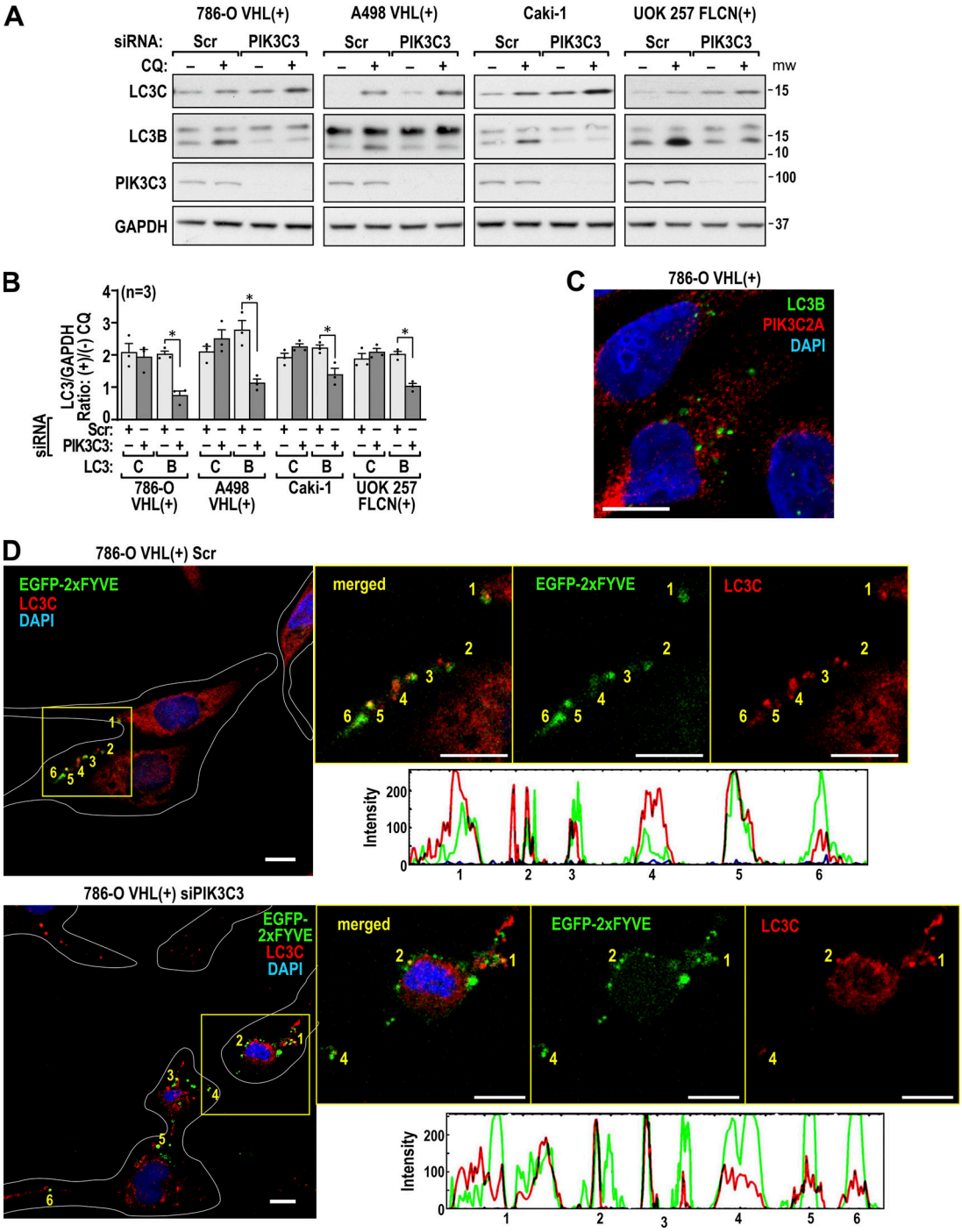

Figure S2. **LC3C is not regulated by PIK3C3. (A)** Immunoblots show that knockdown of PIK3C3 does not inhibit LC3C flux but is effective toward LC3B. **(B)** Quantification of LC3C and B accumulation presented as the ratio of their protein levels normalized to GAPDH in CQ(+) versus CQ(–) in cells transfected with scramble (Scr) or PIK3C3 siRNAs in the indicated cell lines. **(C)** Lack of colocalization of LC3B and PIK3C2A. **(D)** Colocalization of LC3C with PI3P reporter EGFP-2xFyve in cells with PIK3C3 knockdown. Examples of split channels and RGB profiles are shown. Scale bars = 10 µm. For all bar graphs, mean ± SEM is shown. *, P < 0.05 by unpaired two-tailed *t* test.

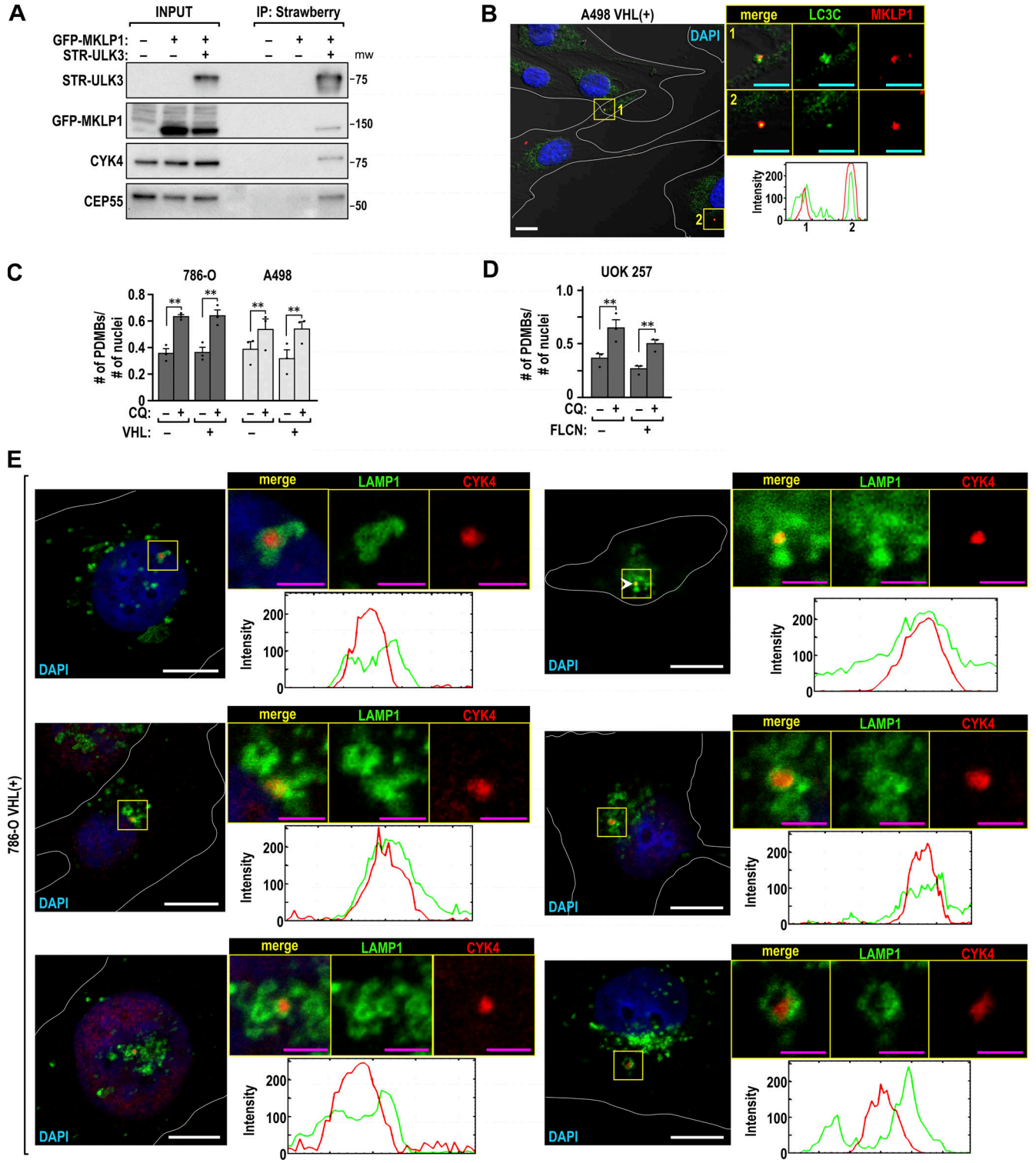

Figure S3. **PDMBs are the target of LC3C autophagy. (A)** STR-ULK3 coimmunoprecipitates midbody proteins MKLP1, CYK4, and CEP55. **(B)** Colocalization of LC3C puncta with PDMBs in A498 VHL(+) cells. RGB profiles and split channels are shown. **(C)** VHL does not affect CQ-dependent degradation of PDMBs under 10% serum conditions. **(D)** FLCN does not affect CQ-dependent degradation of PDMBs under 10% serum conditions. In C and D, quantification was performed as described in Fig. 6 D. **(E)** Multiple examples of colocalization of PDMBs with LAMP1, a lysosomal marker. RGB profiles and split channels are shown. Scale bars are as follows: white = 10 µm; cyan = 5 µm; magenta = 2.5 µm. For all bar graphs, mean ± SEM is shown. **, $P < 0.01$ by unpaired two-tailed *t* test.

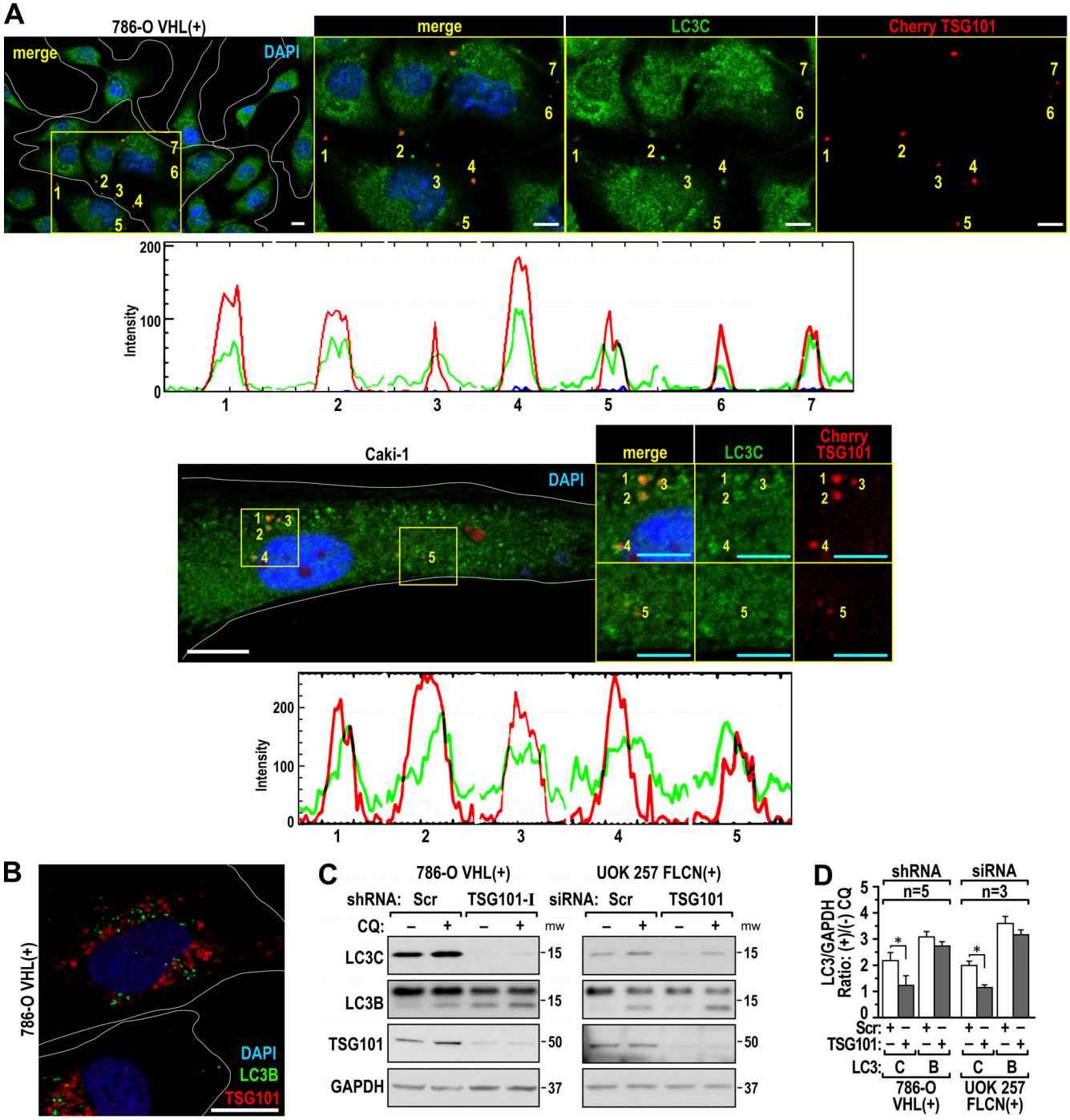

Figure S4. **TSG101 is required for LC3C-dependent degradation of PDMBs. (A)** Cherry-TSG101 colocalizes with endogenous LC3C in 786-O VHL(+) and Caki-1 cells. RGB profiles and split channels are shown. **(B)** Cherry-TSG101 does not colocalize with endogenous LC3B. **(C)** Knockdown of TSG101 inhibits LC3C autophagy. **(D)** Quantification of the LC3C and B accumulation presented as the ratio of their protein levels normalized to GAPDH in CQ(+) versus CQ(−) in cells transfected with scramble (Scr) or TSG101 siRNA or shRNA in the indicated cell lines. Scale bars are as follows: white = 10 µm; cyan = 5 µm. For bar graphs, mean ± SEM is shown. *, P < 0.05 by unpaired two-tailed *t* test.

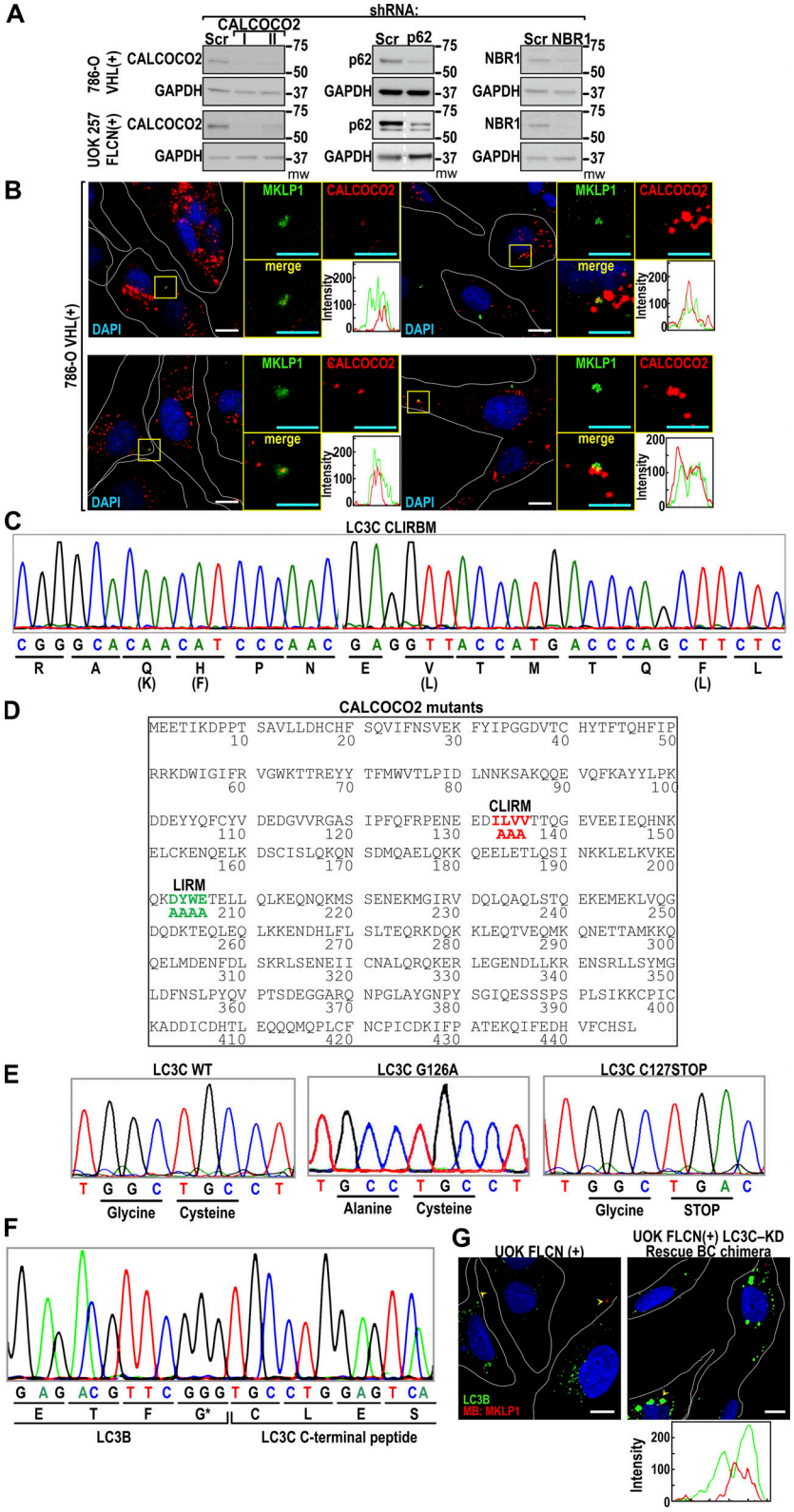

Figure S5. **Selectivity of LC3C autophagy requires LIR-binding motif and LIR on CALCOCO2. (A)** Immunoblots showing knockdowns of respective cargo receptors. **(B)** Representative examples of colocalization of PDMBs with endogenous CALCOCO2. RGB profiles and split channels are shown. MKLP1 is used as a PDMB marker. **(C)** Sequence of LC3C with mutations in CLIR-binding site (CLIRBM). The WT sequence is indicated in parentheses. **(D)** Mutations of CLIR (CLIRM) and LIR (LIRM) motifs in CALCOCO2. Optimized CALCOCO2 was a synthetic gene. **(E)** Sequence of the G126A and C127Stop mutants. **(F)** Sequence of BC chimera. **(G)** Representative examples of immunofluorescence experiments showing lack of colocalization of PDMBs with LC3B in cells with LC3C knockdown (left), but appearance of close proximity and colocalization in cells expressing BC chimeras (right) in UOK 257 cells. RGB profiles are shown. Scale bars are as follows: white = 10 µm; cyan = 5 µm. KD, knockdown; Scr, scramble.

Table S1 is provided online as a separate Word file and lists the reagents used in this study.